



Influence of Gd³⁺ ion doping on structural, optical, and magnetic properties of (Mg–Ni–Co) nanoferrites

Amani Aridi · Mariam Rabaa · Ramy Moussa ·
Rodaina Sayed Hassan · Nader Yaacoub ·
Ramadan Awad

Received: 29 June 2023 / Accepted: 24 October 2023 / Published online: 7 November 2023
© The Author(s), under exclusive licence to Springer Nature B.V. 2023

Abstract The characterization of (Mg–Ni–Co) nanoferrites doped with small different concentrations of gadolinium rare earth metal (Gd³⁺), prepared by the chemical co-precipitation method, is reported in this study. The XRD results reveal that the crystallite sizes, which are close to the particle size detected from TEM analysis, decrease upon adding Gd³⁺. Furthermore, the lattice constant *a* increases from 8.351 to 8.367 Å as the Gd³⁺ concentration (*x*) increases from 0.00 to 0.08.

Highlights

- (Mg–Ni–Co) nanoferrites doped with Gd³⁺ were synthesized by the coprecipitation method.
- Doping the (Mg–Ni–Co) nanoferrites with Gd³⁺ increases the lattice constant and reduces the particle size and saturation magnetization.
- Raman analysis has verified the existence of active modes related to the spinel ferrite structure.
- Referring to the Mössbauer analysis, Gd³⁺ ions occupy the octahedral sites.

A. Aridi (✉) · M. Rabaa
Department of Chemistry, Faculty of Science, Beirut Arab
University, Beirut, Lebanon
e-mail: a.aridi@bau.edu.lb

A. Aridi
Inorganic and Organometallic Coordination Chemistry
Laboratory, Faculty of Sciences I, Lebanese University,
Hadath, Lebanon

R. Moussa · R. Awad
Department of Physics, Faculty of Science, Alexandria
University, Alexandria 21511, Egypt

HRTEM images reveal the presence of different grains with different lattice plane orientations. Furthermore, the appearance of concentric circles in the SAED patterns verified the samples' polycrystalline nature. The presence of the active modes of the spinel structure was confirmed by the Raman analysis with a slight shift upon increasing the Gd³⁺ concentrations. Moreover, the photoluminescence (PL) analysis revealed the presence of a sharp peak in the UV region and structural defects in the prepared samples. Mössbauer spectroscopy and vibrating sample magnetometer (VSM) were used to examine the magnetic properties of the prepared samples. From the Mössbauer analysis, it was suggested that Gd³⁺ ions occupy the octahedral site. In addition, the saturation magnetization (*M_s*) and magnetocrystalline anisotropy (*K*) decreased from 31.87 to 15.76 emu/g and from 0.0057 to 0.0014 J/m³ with the increase of Gd³⁺ concentration from 0.00 to 0.08, respectively. Finally, different forms of the law of approach to saturation (LAS) for ferromagnetic materials were used for the fitting of M–H hysteresis loops at high applied fields. The obtained results show that the LAS model, mainly $M = M_s \left(1 - \frac{b}{H^2} \right) + \chi H$, can

R. S. Hassan
Department of Physics, Faculty of Science, Lebanese
University, Beirut, Lebanon

N. Yaacoub
IMMM, Université du Mans, CNRS UMR-6283, Avenue
Olivier Messiaen, 72085 Le Mans, France

effectively describe the doping of Gd^{3+} for all concentrations. This model exhibits well-fitting with high R^2 values and provides relevant values of the magnetic parameters.

Keywords Spinel ferrites · Gd doping · Raman spectroscopy · Mössbauer spectroscopy · Law of approach to saturation · Magnetism · Nanocomposites

Introduction

The unique structural properties of pure spinel nanoferrites, characterized by the formula MFe_2O_4 (where M represents metal cations such as Mg^{2+} , Ni^{2+} , and Co^{2+}), can be attributed to their special resilience orientation and valence changeability of metal cations with rich surface-active sites [1]. However, certain modifications are required to improve the physical properties of spinel nanoferrites, including low saturation magnetization and chemical stability [2].

Among various types of ferrites, magnesium nanoferrite is highly significant. It is characterized as a soft magnetic n-type semiconducting material with a cubic normal spinel structure. It is widely used in magnetic technologies, electronic materials for nanodevices, storage devices, and catalysis [3]. Due to its typical ferromagnetic characteristics, abundance in nature, strong electrochemical stability, low conductivity, and catalytic action, the soft inverse nickel ferrite is one of the most useful and technologically significant nanoferrites [4]. Cobalt ferrite nanoparticles are a well-known moderate hard magnetic material with a small crystal size, moderate-high saturation magnetization, strong magneto-crystalline anisotropy, and moderate coercivity [5–7]. It crystallizes as the inverse spinel structure, and is used in magnetic recording applications such as audio and video tape, high-density digital recording disks, and physical and chemical durability [8].

The magnetic properties of nickel-substituted cobalt ferrite demonstrated that the change in coercivity, saturation magnetization, remanent magnetization, and squareness ratio was correlated with the amount of nickel. Because nickel has a lower magnetic moment compared to cobalt, the magnetic properties gradually decreased as the amount of nickel substitution increased. The coercive field decreased from 7134 to 279 Oe at 30 K as the nickel content

increased from 0 to 1 in $\text{Co}_{1-x}\text{Ni}_x\text{Fe}_2\text{O}_4$ nanoparticles [9]. Moreover, the increase in the saturation magnetization and remanent magnetization increased as the nickel content increased up to 0.4 was owed to the increase in crystallite size [9, 10]. Doping cobalt ferrite with magnesium reduced the value of saturation magnetization from 37 to 29 emu/g as x increased from 0 to 0.25 in $\text{Co}_{1-x}\text{Mg}_x\text{Fe}_2\text{O}_4$ nanoparticles [11]. Furthermore, the remanent magnetization, the coercivity, and the magnetic moment were diminished as well [11]. The conversion of the magnetic characteristics of cobalt ferrite from moderately hard to soft magnetic materials upon doping it with magnesium is reported in a previous study [12]. Magnesium-doped nickel ferrite showed a growth of crystallite size and a decrease in the anisotropy. In addition, the value of the lattice constant increased from 8.309 to 8.456 Å with the increase in Mg^{2+} concentration [13]. Ashrafizadeh et al. [14] reported that the substitution of magnesium by copper in the $(\text{Mg}_{0.5}\text{Zn}_{0.5})$ ferrites with the composition of $\text{Cu}_x\text{Mg}_{0.5-x}\text{Zn}_{0.5}\text{Fe}_2\text{O}_4$ did not significantly change the average magnetic hyperfine field. The saturation magnetization and magnetic susceptibility were improved by increasing copper concentrations. In addition, the coercive force was decreased by copper ions dopant. Suo et al. [15] synthesized $\text{Ni}_{0.2}\text{Mg}_{0.2}\text{Co}_x\text{Zn}_{0.6-x}\text{Fe}_2\text{O}_4$ ($x = 0, 0.15, 0.3, 0.45$ and 0.6) nanoferrites and found that they had soft magnetic properties. The remanent magnetization, coercivity, and anisotropy constant have increased with the increase of Co^{2+} ion content. Suo et al. [16] declared that the Bi^{3+} doping reduced the magnetic properties in the ferromagnetic $\text{Ni}_{0.2}\text{Mg}_{0.2}\text{Co}_{0.6}\text{Fe}_{2-x}\text{Bi}_x\text{O}_4$ ($x = 0, 0.025, 0.05, 0.075$, and 0.1) nanoparticles.

The incorporation of rare earth metal ions through doping in nanoferrites is an effective method employed to enhance their magnetic, optical, and structural properties [17]. These metal ions exhibit a wide range of magnetic moments and can be arranged in the tetrahedral and octahedral sites in the spinel lattice, leading to improvements in the overall characteristics of the nanoferrites and enabling their utilization in various applications [18, 19]. In the orbital shape of rare earth ions, the unpaired 4f electrons energy level that appeared is the key aspect for originating magnetic anisotropy [20]. The findings of the research done on the substitution of rare earth elements in spinel ferrites with different

concentrations revealed that low concentrations of Gd^{3+} could improve the properties of spinel ferrites and create a distinctive product [21]. Shao et al. [22] reported that $Ni_{0.2}Mg_{0.2}Co_{0.6}Fe_2O_4$ nanoferrites doped with rare-earth ions, mainly La^{3+} , Ce^{3+} , Pr^{3+} , and Sm^{3+} , were suitable for magnetic storage and magnetic recording materials. It had high coercivity, a large squareness ratio (M_r/M_S) and large crystal anisotropy compared to the pure sample. Yu et al. [23] reported that the magnetic properties of $Ni_{0.2}Mg_{0.1}Co_{0.7}Fe_{2-x}Y_xO_4$ nanoferrites can be optimized by adding a small amount of Y^{3+} ions. Consequently, the saturation magnetization increased to 31.09 emu/g with the increase of Y^{3+} concentrations to 0.02 and then decreased to reach 25.54 emu/g with a further increase in Y^{3+} up to 0.08.

Among spinel ferrite nanoparticles, $MgFe_2O_4$ is recognized as a soft magnetic semiconductor, featuring a normal spinel structure [24]. Similarly, $NiFe_2O_4$ is a soft magnetic semiconductor with an inverse spinel structure [25]. In contrast, $CoFe_2O_4$ possesses an inverse spinel structure and is classified as a semi-hard material [26]. Thus, exploring the properties of ferrite nanoparticles, obtained by combining Mg, Co, and Ni metals in equal proportions proves to be an interesting study. Knowing that combining the metals in equal proportions can lead to a synergistic effect, where the prepared nanoparticles can exhibit superior properties compared to $MgFe_2O_4$, $NiFe_2O_4$, and $CoFe_2O_4$ nanoparticles. It is worth mentioning that the choice of the nanoferrite preparation method depends on both the desired properties of the ferrite and its intended application [27, 28]. Furthermore, the influence of Gd^{3+} ion doping on the structural, optical, and magnetic properties of (Mg–Co–Ni) nanoferrites represents a novel approach that has not been explored in previous research. Therefore, spinel $Mg_{0.33}Ni_{0.33}Co_{0.33}Fe_{2-x}Gd_xO_4$ nanoferrites, with $0.00 \leq x \leq 0.08$, were prepared by the co-precipitation method. This synthesis process is known for its simplicity and low cost and allows the control of the grain size and particle size distribution. Several characterization techniques were used to investigate the properties of the prepared samples. To examine the structural properties, X-ray powder diffraction (XRD), transmission electron microscope (TEM), high-resolution transmission electron microscope (HRTEM), selected area electron diffraction (SAED), and Raman spectroscopy were employed. However,

the photoluminescence (PL) analysis provides information about the optical properties, whereas the identification of the magnetic properties was achieved through Mössbauer spectroscopy and M-H loop analysis.

Experimental methods

Materials

Highly pure (above 98%) chemical reagents, mainly magnesium chloride hexahydrate ($MgCl_2 \cdot 6H_2O$), nickel (II) chloride hexahydrate ($NiCl_2 \cdot 6H_2O$), cobalt (II) chloride hydrate ($CoCl_2 \cdot H_2O$), iron (III) chloride hexahydrate ($FeCl_3 \cdot 6H_2O$), gadolinium (III) chloride hexahydrate ($GdCl_3 \cdot 6H_2O$), and sodium hydroxide (NaOH) were used for the preparation of $Mg_{0.33}Ni_{0.33}Co_{0.33}Fe_{2-x}Gd_xO_4$ nanoferrites with $0.00 \leq x \leq 0.08$.

Synthesis method

$Mg_{0.33}Ni_{0.33}Co_{0.33}Fe_{2-x}Gd_xO_4$ nanoparticles were prepared by the co-precipitation method. For the preparation of 25 g of pure $Mg_{0.33}Ni_{0.33}Co_{0.33}Fe_2O_4$ nanoparticles, 2.21, 2.58, 2.59, and 17.62 g of $MgCl_2 \cdot 6H_2O$, $NiCl_2 \cdot 6H_2O$, $CoCl_2 \cdot H_2O$, and $FeCl_3 \cdot 6H_2O$, respectively, were dissolved in deionized water. However, to synthesize $Mg_{0.33}Ni_{0.33}Co_{0.33}Fe_{2-x}Gd_xO_4$ nanoparticles with $0.01 \leq x \leq 0.08$, the amount of $FeCl_3 \cdot 6H_2O$ and $GdCl_3 \cdot 6H_2O$ ranges between 16.74 and 17.51 g and between 0.12 and 0.96 g, respectively. The solutions were then mixed and stirred magnetically for 30 min. The mixture was titrated with NaOH (3M) until it reached a pH of 12. The solution was then maintained at 80 °C for 2 h while stirring magnetically at a constant rate. The obtained precipitates were washed several times with a solution composed of 75% deionized water and 25% ethanol until the pH of the filtrate dropped to 7. The collected samples were dried at 100 °C for 18 h. Finally, the samples were annealed for 4 h at 550 °C.

Characterization techniques

The structure of the prepared samples was determined from the XRD analysis. Therefore, 1 g of each of the prepared nanoparticles was ground to create

a uniform fine-grain powder. This powdered sample was then placed in a plate-shaped holder and subsequently analyzed using a Panalytical Co. Xpert Pro diffractometer. The diffractometer was operated at 45 kV and 40 mA, with Cu-K α X-ray source of radiation ($\lambda = 1.5406 \text{ \AA}$) in the range $20^\circ \leq 2\theta \leq 80^\circ$ with the gradual increase by 0.02° . The obtained XRD patterns were refined by the Rietveld method, using the Material Analysis Using Diffraction (MAUD) software. The morphology, particle size distribution, and crystallinity of synthesized nanoparticles were investigated by TEM, HRTEM, and SAED analysis via the JEOL JEM-2100 operated at 200 kV. This was done by dissolving 10 mg of the nanoparticles in a solution of 50% diluted hydrochloric acid (HCl). Then, the mixture was subjected to 20 min of sonication. Subsequently, a few drops of the suspension were deposited onto a carbon-coated copper grid and left to air-dry at room temperature for several hours. The particle size, distance between the lattice planes, and diameter of the rings were determined from the obtained TEM, HRTEM, and SAED images by using the ImageJ software. Then, Origin Lab software was used to draw the particle size distribution and then it was fitted using the Gaussian function. The Raman analysis was performed at room temperature using a dispersive Raman spectrometer (SENTERRA, Bruker Optics). The Raman spectra were obtained after depositing the powder samples in a silicon reference material under a laser excitation source at a wavelength of 785 nm. The PL spectra were recorded at room temperature by FP-8600 spectrofluorometer, equipped with a Xenon lamp, in the range 320–700 nm at an excitation wavelength of 290 nm. The samples were prepared for the PL analysis by dissolving 3 mg of the nanoparticles in 20 mL of diluted HCl solution. Then, a rectangular quartz cuvette of a path length of 1 cm was used as a sample holder. Finally, the peaks of the PL spectra were deconvoluted via the Fityk program. Additionally, the Mössbauer spectra were recorded at 300 K and 77 K using $^{57}\text{Co/Rh}$ γ -ray source mounted on an electromagnetic transducer with a triangular velocity form. It is worth mentioning that the hyperfine structure was modeled by a least-square fitting method involving Zeeman sextets and quadrupolar doublets comprising Lorentzian lines. Finally, a vibrating sample magnetometer (VSM) (Lake Shore 7410) was used for estimating the magnetic properties. About 0.1 g of

the prepared samples is weighed and mounted on an insulated tube constructed of nonmagnetic material, a quartz tube, in the gap between an electromagnet. The M-H hysteresis loops were recorded in the field range from 20 to 20 kg.

Results and discussion

X-ray powder diffraction analysis

Figure 1 depicts Rietveld refinements of XRD that were performed to confirm the phase purity and crystallinity of the prepared $\text{Mg}_{0.33}\text{Ni}_{0.33}\text{Co}_{0.33}\text{Fe}_{2-x}\text{Gd}_x\text{O}_4$ nanoparticles where $x = 0.00, 0.01, 0.02, 0.04,$ and 0.08 . Following the standard sheet number JCPDS:77-0013, the diffraction peaks located at 2θ of $30.05^\circ, 35.75^\circ, 37.05^\circ, 43.11^\circ, 53.73^\circ, 57.21^\circ,$ and 62.77°

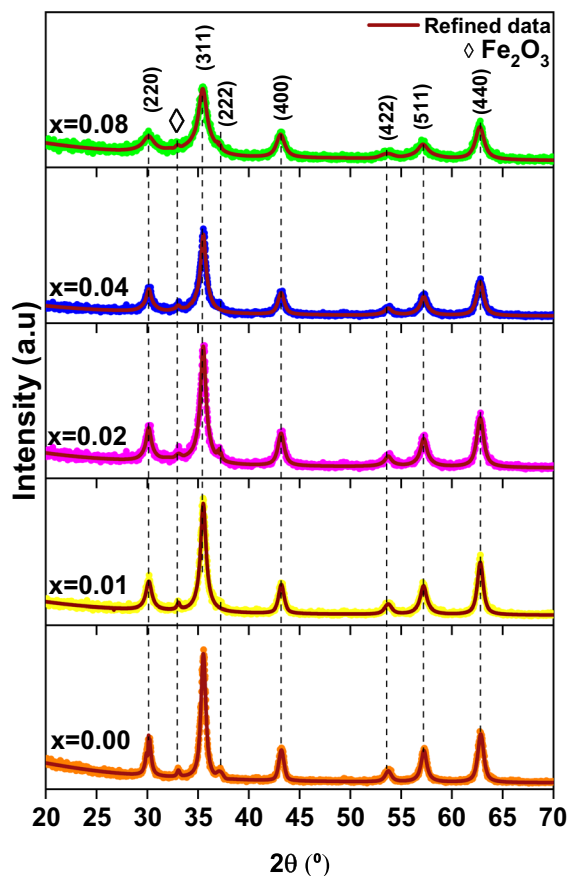


Fig. 1 XRD refinements of $\text{Mg}_{0.33}\text{Ni}_{0.33}\text{Co}_{0.33}\text{Fe}_{2-x}\text{Gd}_x\text{O}_4$ where $x = 0.00, 0.01, 0.02, 0.04,$ and 0.08

were identified as the (220), (311), (222), (400), (422), (511), and (440) planes, respectively [29]. Thus, the prepared nanoferrites crystallize in the FCC crystal structure. A minor peak appeared at $2\theta \sim 33^\circ$ which assigns the presence of the Fe_2O_3 impurity phase which is usually accompanied by ferrite preparation.

The lattice constant a was measured for all the prepared samples and listed in Table 1 according to the following equation [30]:

$$\frac{1}{d^2} = \frac{h^2 + k^2 + l^2}{a^2}, \tag{1}$$

where h , k , and l are Miller indices and d is the space between the planes. It is clear, from Table 1, that the calculated a values show a remarkable increase with increasing the Gd^{3+} concentrations. This is well consistent with Vegard’s law [31]. This finding is mainly due to the difference in ionic radii between Gd^{3+} (0.938 Å) and Fe^{3+} (0.645 Å) which could result in an enhancement in the unit cell parameter a of the prepared Mg–Ni–Co nanoferrites. The crystallite sizes of the produced Mg–Ni–Co doped with Gd^{3+} ion nanoferrites were estimated for the most intense peak (311) plane determined from the XRD data, using the Debye-Scherrer’s formula [32]:

$$D = \frac{\alpha\lambda}{\beta\cos\theta}, \tag{2}$$

where λ is the wavelength of the Cu target (1.5406 Å), β is the full width of half maximum (FWHM) of the most intensive diffraction peak (311), and 2θ is the diffraction angle. It can be seen from Table 1 that the crystallite

sizes showed a significant decrease from 30.27 to 23.39 nm with increasing the Gd^{3+} concentration. Additionally, the observed broadening of the (311) peak with increasing substitution content is a good indication of Gd^{3+} incorporation in the Mg–Ni–Co nanoferrite lattice. This incorporation should result in a reduction in crystallite sizes [33]. The decrease of the particle size upon doping nanoferrites with Gd is attributed to the reduction in the surface energy which in turn prevents the growth of nanoparticles [34]. The dislocation density (δ), the X-ray density (ρ_x), the specific surface area (S), strain (ϵ), and polaron radius (γ_p), listed in Table 1, were calculated using the following relations, respectively [35, 36]:

$$\delta = \frac{1}{D^2}, \tag{3}$$

$$\rho_x = \frac{8M}{N_A a^3}, \tag{4}$$

$$S = \frac{6}{\rho_x D}, \tag{5}$$

$$\epsilon = \frac{\beta\cos\theta}{4}, \tag{6}$$

$$\gamma_p = \frac{1}{2} \sqrt[3]{\frac{\pi a^3}{576}}, \tag{7}$$

where M is the molecular weight and N_A is Avogadro’s number. The concentration of lattice imperfections,

Table 1 Structural parameters valued from XRD and TEM analysis for $\text{Mg}_{0.33}\text{Ni}_{0.33}\text{Co}_{0.33}\text{Fe}_{2-x}\text{Gd}_x\text{O}_4$ nanoparticles with $0.00 \leq x \leq 0.08$

x	0.00	0.01	0.02	0.04	0.08
a (Å)	8.351(3)	8.361(9)	8.362(9)	8.364(9)	8.367(8)
D_{XRD} (nm)	30.27	27.8	26.05	25.26	23.39
$\delta \times 10^{-3}$ (nm^{-2})	9.90	10.7	11.4	11.8	12.6
ρ_x (g/cm^3)	4.955	5.092	5.118	5.155	5.242
S (m^2/g)	39.999(3)	42.383(6)	44.995(5)	46.069(9)	48.930(6)
ϵ	0.166(8)	0.166(3)	0.166(4)	0.166(2)	0.165(2)
L_A (Å)	3.616(2)	3.620(8)	3.621(2)	3.622(1)	3.623(3)
L_B (Å)	2.952(6)	2.956(3)	2.956(7)	2.957(4)	2.958(4)
γ_P (Å)	0.735(0)	0.735(9)	0.736(0)	0.736(2)	0.736(4)
D_{TEM} (nm)	27.5	23.3	20.1	18.7	14.2

known as dislocation density δ , is influenced by the concentration of Gd^{3+} and is inversely proportional to particle size. Consequently, as the Gd^{3+} content increases, the dislocation density δ increases. Similar results were reported upon doping $\text{Ni}_{0.5}\text{Zn}_{0.5}\text{Fe}_2\text{O}_4$ with ruthenium [37]. As listed in Table 1, the linear increase in ρ_x from 4.955 to 5.242 g/cm^3 by increasing the concentration of the Gd^{3+} is attributed to the increase in the molecular weight of the prepared samples [38]. Additionally, the surface area (S) increases from 39.99 to 43.93 m^2/g upon increasing the Gd^{3+} content from 0.00 to 0.08. This is owed to the inverse proportionality between the surface area and the crystallite size [39]. Upon doping nanoferrites with Gd^{3+} , the strain ϵ values, mentioned in Table 1, are slightly reduced. This might be attributed to the difference in ionic radii of the Gd^{3+} (0.938 Å) and Fe^{3+} (0.645 Å) [40, 41]. When Gd^{3+} ions substitute for the host Fe^{3+} ions, the larger size of Gd^{3+} causes an expansion of the crystal lattice. This increase in the lattice parameter reduces the strain and subsequently decreases the microstrain [42]. The distance between magnetic ions (hopping length) in the tetrahedral and octahedral sites is given by [35]:

$$L_A = a \frac{\sqrt{3}}{4} \quad (8)$$

$$L_B = a \frac{\sqrt{2}}{4}. \quad (9)$$

As declared in Table 1, the values L_A and L_B increase with increasing the substitution of Fe^{3+} by Gd^{3+} ions and lattice parameter. This is owed to the fact that the hopping length referring to the A-B sites is longer than that of the A-A and B-B sites [36]. The polaron radius slightly increases from 0.735(0) to 0.736(4) Å by increasing the Gd^{3+} concentration from 0.00 to 0.08. This is owed to the electron-phonon interaction as the charge carriers are confined in the d-shell. This polaron defect appeared because of the moving of the neighboring atoms from their position immediately after the charge carriers get caught in the lattice site [43].

To compare the obtained results with those reported in previous studies, the structural parameters of pure and Gd-doped MgFe_2O_4 , NiFe_2O_4 , and CoFe_2O_4 are listed Table 2. It is worth mentioning that the preparation method and cationic distribution affect the structural parameters of ferrite nanoparticles. Smaller crystallite sizes are obtained in this study. However, comparable values of L_A and L_B were reported for NiFe_2O_4 and MgFe_2O_4 nanoparticles [44, 45]. Additionally, an increasing trend in the lattice parameter accompanied by a shrinking trend in the crystallite size was observed upon increasing the Gd^{3+} content in $\text{CoFe}_{2-x}\text{Gd}_x\text{O}_4$, $\text{NiFe}_{2-x}\text{Gd}_x\text{O}_4$ and $\text{Gd}_x\text{MgFe}_{2-x}\text{O}_4$ [47–49]. This was attributed to the difference in the ionic radius between the Gd^{3+} ions and Fe^{3+} ions and the act of Gd^{3+} as a restraint to

Table 2 Structural parameters of pure and Gd-doped nanoferrites reported in the literature

Nanoparticle		a (Å)	D_{XRD} (nm)	$\delta \times 10^{-3}$ (nm^{-2})	ϵ	L_A (Å)	L_B (Å)	Ref.
NiFe_2O_4		8.3402	54.57	0.34	0.064	3.6114	2.9482	[44]
MgFe_2O_4		8.376	20.89	2.290	0.0951	3.627	2.961	[45]
CoFe_2O_4		8.362	21	1.354	0.1583	–	–	[46]
$\text{CoFe}_{2-x}\text{Gd}_x\text{O}_4$	$x=0.00$	8.365	77.37	–	–	–	–	[47]
	$x=0.03$	8.371	32.56	–	–	–	–	
	$x=0.09$	8.388	23.26	–	–	–	–	
	$x=0.12$	8.376	22.13	–	–	–	–	
	$x=0.15$	8.377	20.82	–	–	–	–	
$\text{NiFe}_{2-x}\text{Gd}_x\text{O}_4$	$x=0.00$	8.365	30.12	–	–	3.6222	2.9575	[48]
	$x=0.025$	8.369	29.15	–	–	3.6239	2.9589	
	$x=0.05$	8.374	26.35	–	–	3.6261	2.9607	
	$x=0.075$	8.378	24.61	–	–	3.6278	2.9621	
	$x=0.1$	8.383	23.25	–	–	3.6299	2.9639	
$\text{Gd}_x\text{MgFe}_{2-x}\text{O}_4$	$x=0.0$	8.4038	24	–	–	–	–	[49]
	$x=0.1$	8.4129	20	–	–	–	–	

the growth process. Therefore, consistent results are obtained in this study.

TEM, HRTEM, and SAED analysis

The morphology and average particle size of $\text{Mg}_{0.33}\text{Ni}_{0.33}\text{Co}_{0.33}\text{Fe}_{2-x}\text{Gd}_x\text{O}_4$ nanoparticles were determined by TEM analysis. The average particle size (D_{TEM}), listed in Table 1, was examined from TEM images (Fig. 2(a₁–e₁)). In addition, the histograms, representing the particle size distribution, are obtained using the ImageJ software and illustrated in Fig. 2(a₂–e₂). The prepared nanoparticles exhibit rounded-cube morphology with a particle size distribution that ranges between 0 to 60 nm. MgFe_2O_4 , NiFe_2O_4 , and CoFe_2O_4 have similar morphologies, according to earlier investigations [50–52]. The average particle size of $\text{Mg}_{0.33}\text{Ni}_{0.33}\text{Co}_{0.33}\text{Fe}_{2-x}\text{Gd}_x\text{O}_4$ nanoparticles is reduced from 27.4 to 14.3 nm as x increases from 0.00 to 0.08, respectively. This decrement in the particle size with increasing the Gd^{3+} concentration is attributed to the act of Gd^{3+} as a restraint to the growth process, causing the formation of smaller particle sizes. These results are in agreement with a previously published paper where the particle size of $\text{Co}_{0.6}\text{Mn}_{0.4}\text{Gd}_x\text{Fe}_{2-x}\text{O}_4$ nanoparticles decreased from 47.88 to 40.97 nm as the Gd content increased from 0 to 0.1 [53]. The change in particle size, as estimated from TEM and XRD analysis, exhibits a consistent trend. However, the smaller values of D_{TEM} compared to D_{XRD} can be attributed to the aging in the reaction solution [54]. The obtained result is similar to a previous study where the particle size estimated from TEM was smaller than that valued from XRD analysis for $\text{Zn}_{0.5}\text{Co}_{0.5}\text{Fe}_{2-x}\text{Pr}_x\text{O}_4$ nanoparticles [55]. All the prepared samples show a degree of agglomeration that may be due to the magnetic interparticle interactions [53, 56]. The HRTEM images, shown in Fig. 2(a₃–e₃), reveal the presence of different grains with different lattice plane orientations. This observation is attributed to the polycrystalline nature of the samples. Additionally, the presence of lattice fringes confirms the crystalline nature of the samples. The values of distance between the lattice planes along with their corresponding miller indices for selected grains are displayed in Fig. 2(a₃–e₃) and are comparable with the XRD results. The selected area of electron diffraction (SAED) images, displayed in Fig. 2(a₄–e₄), reveals the presence of concentric

circles which confirms the polycrystalline nature of the samples. The identified planes mainly (220), (311), (222), (400), (422), (551), and (440) are in agreement with those obtained from XRD measurements. Thus, the SAED images with the identified planes confirm the formation of the desired spinel ferrite nanoparticles.

Raman analysis

Raman spectra of $\text{Mg}_{0.33}\text{Ni}_{0.33}\text{Co}_{0.33}\text{Fe}_{2-x}\text{Gd}_x\text{O}_4$ nanoparticles ($x = 0.00, 0.02, \text{ and } 0.08$) were recorded in the wavenumber range of 125–800 cm^{-1} . The prepared nanoferrites belong to the Fd-3m space group, which has an alternating A-B sublattice made up of 56 atoms in the entire unit cell and 14 atoms in the smallest Bravais lattice [57]. The obtained spectra comprise the Raman active modes associated with the formation of the spinel ferrite nanoparticles. The analysis of group theory of the lattice vibrations reveals Raman active modes where A , E , and T represent one-, two-, and three-dimensional Raman modes, respectively [58]. Clearly, all the samples exhibit more than five Raman active modes. The appearance of additional modes is ascribed to the vibrations of various cations, mainly Fe, Mg, Ni, Co, and Gd, each with distinct properties [59].

The Raman spectra were deconvoluted to get more specific details about the lattice structure and the vibrational modes by the Gaussian superposition fitting method using OriginLab software. The resulting deconvoluted spectra are shown in Fig. 3. In addition, Table 3 summarizes the Raman mode's peak position of $\text{Mg}_{0.33}\text{Ni}_{0.33}\text{Co}_{0.33}\text{Fe}_{2-x}\text{Gd}_x\text{O}_4$ for $x = 0.00, 0.02, \text{ and } 0.08$. The detected Raman modes are attributed to the different cations that can occupy an identical position with the same lattice structure [60]. Furthermore, the broadening of certain peaks and the presence of weak modes are ascribed to the formation of small-sized ferrite nanoparticles [61]. The represented active modes confirm the spinel phase formation and are in good agreement with previously published reports [62, 63]. The variation of Raman peak position upon doping nanoferrites with Gd^{3+} gives information about the deformation and the rearrangement of cations and anions in the lattice structure [64].

Vibrational modes observed above 600 cm^{-1} in the Raman spectrum were assigned to vibrations within the

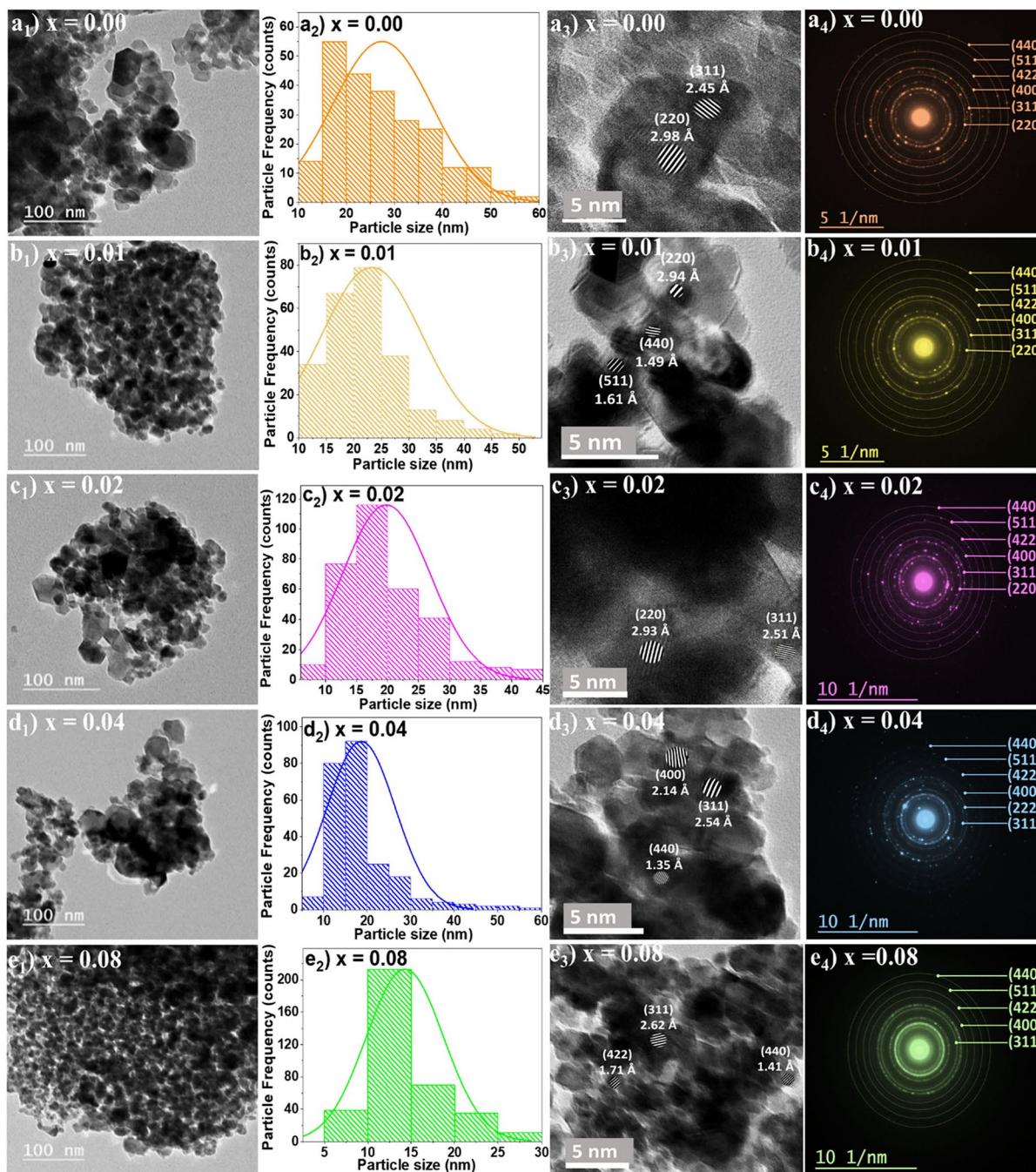


Fig. 2 TEM images (a_1 – e_1), histograms of the particle size distribution (a_2 – e_2), HRTEM image (a_3 – e_3), and SAED images (a_4 – d_4) of $\text{Mg}_{0.33}\text{Ni}_{0.33}\text{Co}_{0.33}\text{Fe}_{2-x}\text{Gd}_x\text{O}_4$ where $0.00 \leq x \leq 0.08$

tetrahedral complex (AO_4). Conversely, those below 600 cm^{-1} were associated with oxygen vibrations within the octahedral complex (BO_6). The A_{1g} mode corresponds to the symmetric stretch of oxygen anion in the tetrahedral

arrangement [65]. The band at A_{1g} mode was deconvoluted into three peaks, which are assigned to Fe–O and M–O where M=Ni and Co [66]. The different cations in the samples are responsible for the presence of the

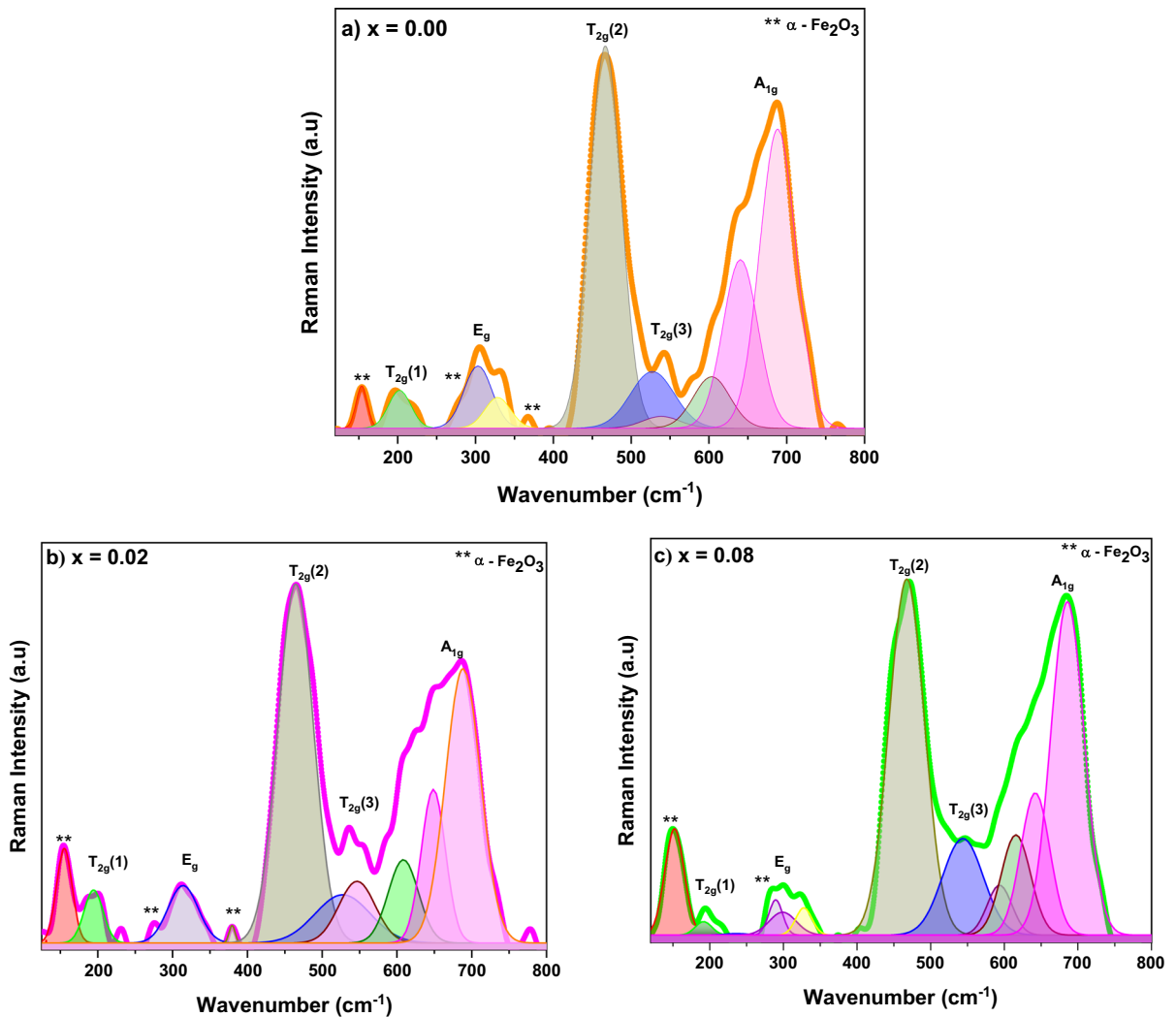


Fig. 3 Deconvoluted Raman spectra of $Mg_{0.33}Ni_{0.33}Co_{0.33}Fe_{2-x}Gd_xO_4$ where **a** $x = 0.00$, **b** 0.02 , and **c** 0.08

Table 3 Raman peaks of $Mg_{0.33}Ni_{0.33}Co_{0.33}Fe_{2-x}Gd_xO_4$ where $x = 0.00, 0.02, \text{ and } 0.08$

x	0.00	0.02	0.08
$T_{2g}(1)$	198	196	192
E_g	311	310	301
$T_{2g}(2)$	464	463	462
$T_{2g}(3)$	542	549	543
A_{1g}	600	601	614
	667	649	648
	688	686	683

shouldered peak in A_{1g} mode because of those movements to the tetrahedral site at the same position [66]. Furthermore, the A_{1g} mode, located between 600 and 750 cm^{-1} , is red-shifted with increasing the Gd^{3+} concentration. This is owed to the dynamic motion of Fe^{3+} in the direction of the A sites [67]. Furthermore, the Raman modes labeled $T_{2g}(3)$ and $T_{2g}(2)$ arise from the symmetric and asymmetric bending vibrations of the oxygen atom within the M–O bond at the octahedral site. The E_g Raman mode corresponds to the symmetric bending motion of the oxygen atom relative to the metal ion located at the octahedral site [68]. Finally, the $T_{2g}(1)$

mode, located in the range of 192–198 cm^{-1} corresponds to the translational movement of the entire MO_4 tetrahedral units [69]. The redshift in the peak related to the A_{1g} band T_{2g} (2) might be attributed to the alteration in the population of Fe^{3+} ions at the tetrahedral and octahedral sites [70]. Interestingly, the peak located $< 200 \text{ cm}^{-1}$ was associated with the A_{1g} mode and two peaks of E_g mode, positioned in the range of 275–305 cm^{-1} and 367–380 cm^{-1} , correspond to the vibrational modes of hematite Fe_2O_3 [71–73]. The recorded Raman spectra show a decrease in peak position by increasing the Gd^{3+} concentrations for all samples as shown in Table 2. This slight redshift may be due to the large difference in reduced mass of Fe^{3+} (55.85 g) and Gd^{3+} (157.25 g) ions causing changes in the M–O (M = Fe, Gd) bonds [41].

PL examination

The optical properties of the synthesized $\text{Mg}_{0.33}\text{Ni}_{0.33}\text{Co}_{0.33}\text{Fe}_{2-x}\text{Gd}_x\text{O}_4$ nanoparticles, where $x=0.00, 0.01, 0.02, 0.04, \text{ and } 0.08$, were investigated via PL spectroscopy performed at room temperature. PL is used to analyze the structural defects in terms of the energy state of sub-energy level defects and the process of emission as well as the excitation. The recorded PL spectra of the prepared samples are shown in Fig. 4. The particle size, surface defects, and oxygen functionalities play a crucial role in the photoluminescent property of the prepared samples [74]. The intensity of the PL signal provides information on the quality of surfaces and interfaces [75]. A sharp peak with the highest intensity of PL emission was detected near 334 nm in the prepared NPs. This is due to the recombination of electron-hole pairs at the defect site due to electron transitions from the valence band to the conduction band. With the increase of Gd^{3+} concentration, the intensity of the PL peak located near 335 nm decreases, along with the appearance of small humps. Furthermore, the slowest recombination rate was detected for $\text{Mg}_{0.33}\text{Ni}_{0.33}\text{Co}_{0.33}\text{Fe}_{2-x}\text{Gd}_x\text{O}_4$ nanoparticles with $x=0.08$. Violet emission, observed at 410 nm, is attributed to the emission from some deep level in the band gap [76]. Furthermore, the blue emission is detected in the range of 435–470 nm and is allocated to the recombination of electrons from vacancies to the holes in the valence band. This phenomenon occurs due to quantum confinement, resulting from the presence of radiative defects located at the surface

grain boundaries of spinel ferrites. In addition, the blue emission band is due to the $3d^5 \rightarrow 3d^4 4s$ transition of Fe^{3+} at tetrahedral sites [77]. The green emission band that appears near 550 nm in the prepared NPs is related to oxygen vacancies or other defects within the crystal lattice [37].

Mössbauer spectroscopy

Figures 5 and 6 display the Mössbauer spectra recorded at 300 and 77 K without an external applied field of $\text{Mg}_{0.33}\text{Ni}_{0.33}\text{Co}_{0.33}\text{Fe}_{2-x}\text{Gd}_x\text{O}_4$ nanoparticles where $x = 0.00, 0.02, \text{ and } 0.08$. The obtained Mössbauer parameters, including the mean values of the isomer shift (IS), quadrupole shift (QS), the hyperfine field (B_{hyp}), and the area percentage (S) are listed in Table 3. Being less than 0.5, the IS values range between 0.305–0.308 mm/s and 0.379–0.489 mm/s at 300 and 77 K, respectively, indicating the existence of Fe^{3+} ions and lack of Fe^{2+} ions [78, 79].

The Mössbauer spectra recorded at 300 K for $x = 0.00$, displayed in Fig. 5a, show a clear magnetic sextet comprising asymmetrical lines. This sextet can be described by at least two magnetic sextets, each having different isomer shift and hyperfine field values based on the iron coordination at the tetrahedral A and octahedral B sites. However, due to the limited resolution of the recorded spectra, it is not possible to achieve a more precise fitting. Therefore, the fitting is performed using a discrete hyperfine field distribution, which allows for the determination of average hyperfine parameter values. As Gd concentration increases from 0.00 to 0.08, an additional central paramagnetic doublet is observed alongside the relaxed sextet as shown in Fig. 5c. This is mainly attributed to the existence of reduced particle sizes in Gd-doped nanoparticles [80]. As x increases from 0.00 to 0.08, average particle size decreases from 27.5 to 14.2 nm along with the decrease in B_{hyp} values. This might be attributed to an increase in the lattice distortion upon doping nanoferrites with Gd^{3+} ions.

The Mössbauer spectra obtained at 77 K, represented in Fig. 6, reveal different hyperfine patterns characterized by well-defined magnetic sextets. Notably, each spectrum can be separated into two prominent sextets. The absence of paramagnetic doublet in Gd-doped nanoferrite ($x = 0.08$) Mössbauer spectrum recorded at 77 K, shown in Fig. 6c, verifies that the doublet observed at 300 K was a result of thermal superparamagnetic

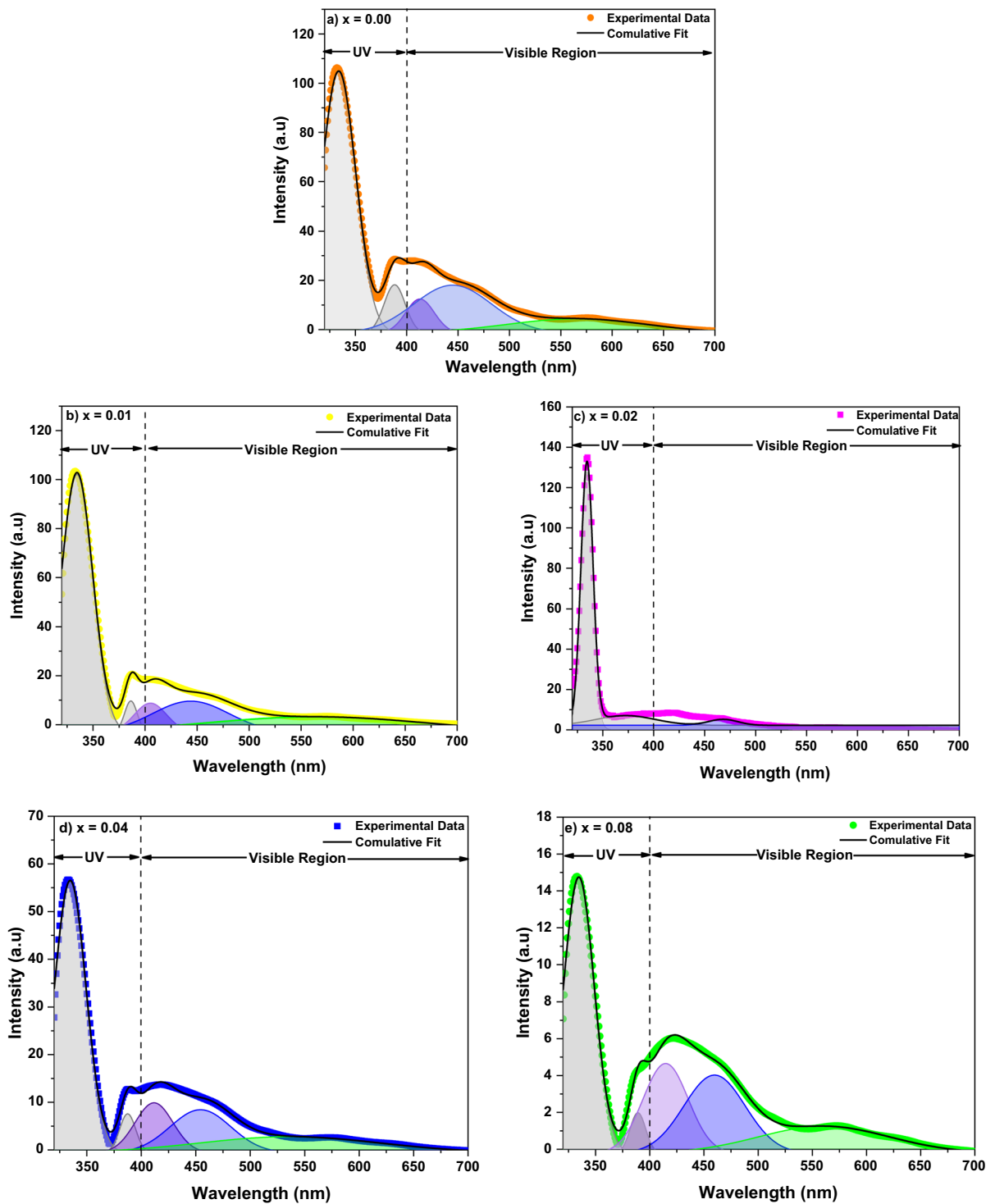


Fig. 4 Deconvoluted PL spectra of $\text{Mg}_{0.33}\text{Ni}_{0.33}\text{Co}_{0.33}\text{Fe}_{2-x}\text{Gd}_x\text{O}_4$ where (a) $x = 0.00$, (b) $x = 0.01$, (c) $x = 0.02$, (d) $x = 0.04$, and (e) $x = 0.08$

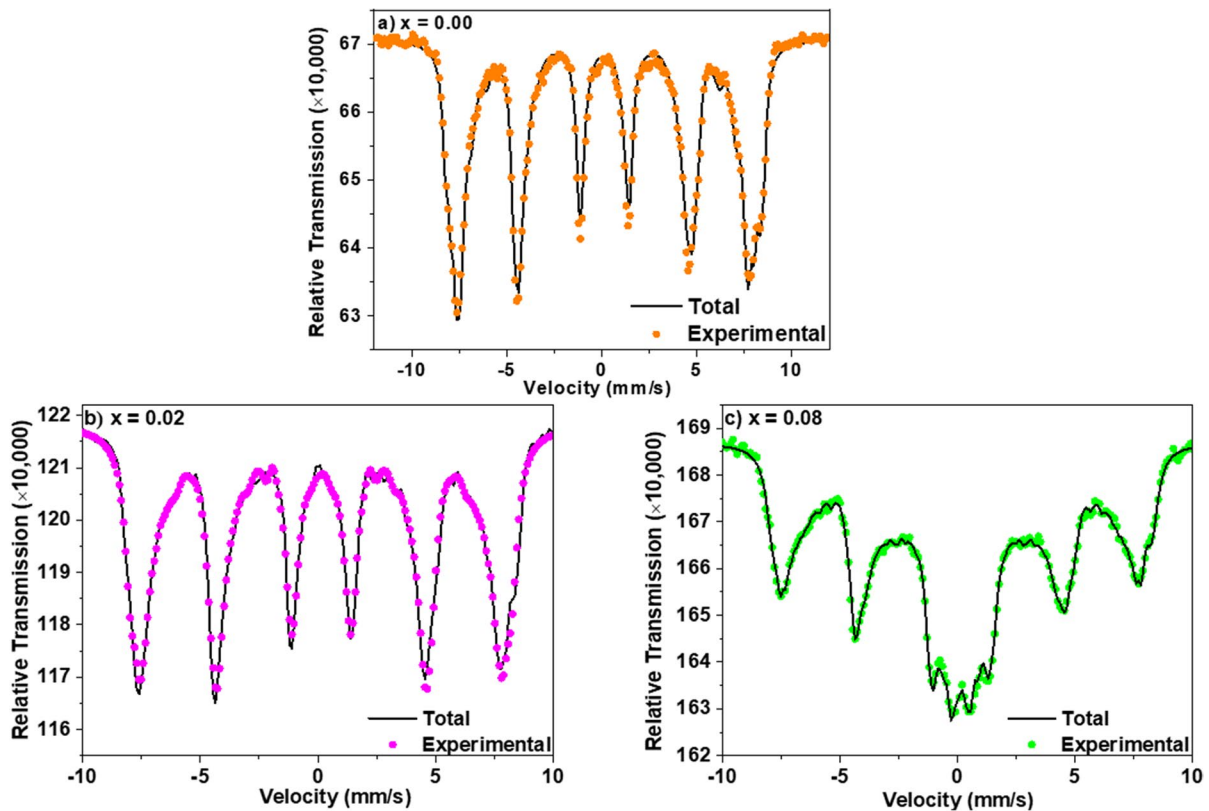


Fig. 5 Mössbauer spectra of $\text{Mg}_{0.33}\text{Ni}_{0.33}\text{Co}_{0.33}\text{Fe}_{2-x}\text{Gd}_x\text{O}_4$ ($x = 0.00, 0.02, \text{ and } 0.08$) samples recorded at 300 K

fluctuations [81]. Furthermore, it is observed that the IS values at the B site are greater than those of the A-site. This phenomenon is attributed to the larger bond separation between $\text{Fe}^{3+}\text{-O}^{2-}$ for the octahedral ions compared to the tetrahedral ions [82]. Knowing that S_B and S_A represent area percentages for B and A sites respectively, the S_B/S_A ratio was determined and listed in Table 4. As Gd concentration increases from 0.00 to 0.08, the S_B/S_A ratio is reduced from 0.82 to 0.43. This can be attributed to the settling of Gd^{3+} dopant ions at the B site causing the migration of Fe^{3+} ions from the octahedral site to the tetrahedral site.

The occurrence of chemical disorder in spinel ferrite structures leads to the generation of an electric field gradient (EFG) which is responsible for the quadrupole splitting (QS) observed in the Mössbauer spectra [83]. The QS values, listed in Table 4, show that the values at examined 300 K are less than that at 77 K. This is owed to the fact that as the temperature of the nanoferrites rises, the thermal energy causes increased atomic movement within the nanoparticle. This

enhanced atomic motion leads to a broader distribution of electric charges, resulting in a reduction in the EFG at the nucleus. Consequently, the quadrupole splitting (QS) observed in the Mössbauer spectra decreases. In comparison to tetrahedral symmetry, octahedral symmetry in crystal structures exhibits a higher degree of asymmetry. Consequently, the larger EFG leads to a larger quadrupole splitting (QS) observed at B sites compared to those at A sites [84]. The small values of QS observed in both the A and B suggest that the local symmetry of the obtained ferrite nanoparticles is closely approaching cubic symmetry [85].

M-H hysteresis loops

The magnetic properties of $\text{Mg}_{0.33}\text{Ni}_{0.33}\text{Co}_{0.33}\text{Fe}_{2-x}\text{Gd}_x\text{O}_4$ nanoparticles were evaluated at room temperature using VSM with a maximum applied field of 20 kG. The obtained M-H hysteresis loops, shown in Fig. 7, were used to estimate the magnetic parameters like saturation magnetization (M_s), retentivity (M_r), coercive force (H_c),

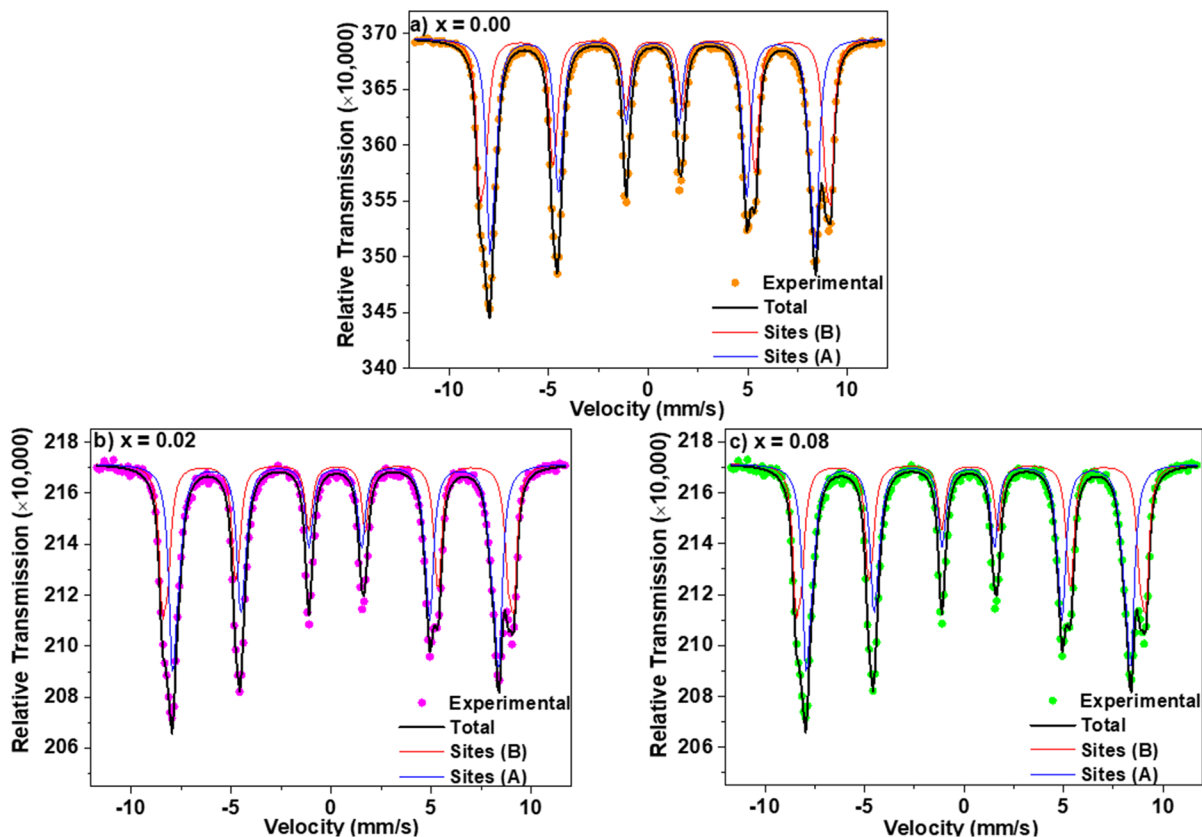


Fig. 6 Mössbauer spectra of $Mg_{0.33}Ni_{0.33}Co_{0.33}Fe_{2-x}Gd_xO_4$ ($x = 0.00, 0.02,$ and 0.08) samples recorded at 77 K

Table 4 Mössbauer parameters of $Mg_{0.33}Ni_{0.33}Co_{0.33}Fe_{2-x}Gd_xO_4$ with $x = 0.00, 0.02,$ and 0.08 recorded at 300 and 77 K

$Mg_{0.33}Ni_{0.33}Co_{0.33}Fe_{2-x}Gd_xO_4$			IS (mm/s)	QS (mm/s)	B_{hyp} (T)	S (%)	S_B/S_A
$T = 300$ K	$x = 0.00$	Sites (A) and (B)	0.308	-0.005	46.9	-	-
	$x = 0.02$	Sites (A) and (B)	0.305	-0.011	34.9	-	-
	$x = 0.08$	Sites (A) and (B)	0.305	0.011	30.7	-	-
$T = 77$ K	$x = 0.00$	Site (B)	0.485	0.056	53.6	45	0.82
		Site (A)	0.379	0.002	50.0	55	
	$x = 0.02$	Site (B)	0.485	0.046	53.5	42	0.72
		Site (A)	0.382	0.004	49.7	58	
	$x = 0.08$	Site (B)	0.489	0.038	53.5	30	0.43
		Site (A)	0.410	0.007	48.7	70	

the squareness ratio ($SQR = M_r/M_s$), and magnetocrystalline anisotropy constant (K). The values of the magnetic parameters are listed in Table 5.

The values of the M_s and H_c for pure $Mg_{0.33}Ni_{0.33}Co_{0.33}Fe_2O_4$ nanoparticles are 31.870 emu/g and 284.89 G, respectively. Naaz et al. [86]

reported lower values for M_s (24.520 emu/g) and H_c (93.78 Oe) for $MgFe_2O_4$ nanoparticles. However, $CoFe_2O_4$ nanoparticles exhibited superior M_s (52.57 emu/g) and H_c (377 Oe) values [87]. Improved M_s value (41.67 emu/g) and lower H_c (0.027 Oe) were reported for $NiFe_2O_4$ nanoparticles in a previous study

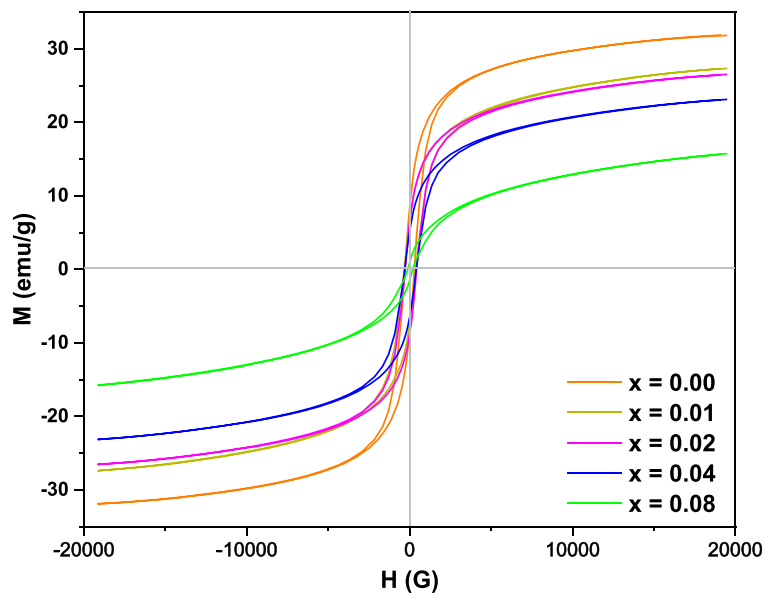


Fig. 7 M-H hysteresis loops of $\text{Mg}_{0.33}\text{Ni}_{0.33}\text{Co}_{0.33}\text{Fe}_{2-x}\text{Gd}_x\text{O}_4$ nanoparticles where $0.00 \leq x \leq 0.08$

Table 5 Magnetic parameters of $\text{Mg}_{0.33}\text{Ni}_{0.33}\text{Co}_{0.33}\text{Fe}_{2-x}\text{Gd}_x\text{O}_4$ where $0.00 \leq x \leq 0.08$

x	M_s (emu/g)	M_r (emu/g)	H_c (G)	SQR	K (J/m ³)
0.00	31.870	8.306	284.89	0.260	0.0057
0.01	27.357	6.357	274.59	0.225	0.0047
0.02	26.524	6.359	276.11	0.239	0.0046
0.04	23.126	5.265	307.05	0.227	0.0044
0.08	15.760	1.137	149.17	0.072	0.0014

[88]. It is worth mentioning that all the mentioned references used the coprecipitation method in the synthesis of MgFe_2O_4 , CoFe_2O_4 , and NiFe_2O_4 nanoparticles. However, the difference in the values of M_s and H_c can be attributed to the cation distribution [89]. Thus, the modification in the nature and concentration of ions in A and B sites causes a variation in the resultant magnetization.

Doping $\text{Mg}_{0.33}\text{Ni}_{0.33}\text{Co}_{0.33}\text{Fe}_{2-x}\text{Gd}_x\text{O}_4$ with different Gd concentrations initiates a significant effect on the magnetic properties of ferrite nanoparticles. The saturation magnetization of the prepared samples decreases from 31.870 to 15.760 emu/g as the concentration of Gd^{3+} increases from 0.00 to 0.08, respectively. The decrease of M_s can be explained by the 4f-3d electron

coupling which refers to the interaction between the localized 4f electrons of the rare earth ions and the 3d electrons of the transition metal ions [48, 90]. Moreover, the weak Gd^{3+} - Gd^{3+} interactions, mainly arising from the indirect 4f-5d-4f mechanism, lead to a reduction in magnetization [91]. Similarly in a previous study, the substitution of magnetic Fe^{3+} ions with non-magnetic Gd^{3+} ions in the B site leads to a reduction in the magnetic moment of the B sublattice and caused a decrease in M_s values in $\text{Ni}_{0.9}\text{Cd}_{0.1}\text{Gd}_x\text{Fe}_{2-x}\text{O}_4$ nanoparticles [92]. Peng et al. [93] reported a decrease in M_s values with the increase of Gd^{3+} concentrations in $\text{CoFe}_2\text{Gd}_x\text{O}_4$ nanoparticles. In addition, the diminishing trend of the M_s was attributed to the variation in the cation distribution upon varying x in the $\text{Co}_x\text{Fe}_{3-x}\text{O}_4/\text{SiO}_2$ system [7]. The magnetocrystalline anisotropy constant K was calculated from the equation [94, 95]:

$$K = \frac{\mu_0 H_c M_s}{2} \quad (9)$$

The calculated values of K , listed in Table 5, showed a decrease with increasing the Gd^{3+} concentration. This may be due to the large magnetic moment Gd^{3+} ($7.94 \mu_B$) ions that replace the smaller Fe^{3+} ($5.92 \mu_B$) ions at B sites [53, 96]. The squareness ratio ($\text{SQR} = M_r/M_s$) values are less than 0.5 revealing

that the prepared samples are formed of single magnetic domain nanoparticles as stated by the Stoner Wohlfarth model [97, 98]. Furthermore, surface effects led to the uniaxial anisotropy in the prepared magnetic nanoferrites [99]. Among the prepared samples, $Mg_{0.33}Ni_{0.33}Co_{0.33}Fe_{2-x}Gd_xO_4$ nanoparticles with $x = 0.04$ exhibited the highest value of coercivity where $H_c = 307.05$ G. This might be ascribed to a higher level of spin-orbit coupling. Also, the enhanced H_c value may be due to the single ion anisotropy of rare-earth ions in the crystal lattice and the surface effects that alter the magnetic structure of nanoparticles [100, 101]. The reduced coercivity value ($H_c = 149.17$ G) revealed by nanoferrites with $x = 0.08$ is related to the small particle size, being below the critical size, as revealed from TEM analysis ($D_{TEM} = 14.2$ nm). Besides, the centered doublet, observed in the Mössbauer spectrum of $Mg_{0.33}Ni_{0.33}Co_{0.33}Fe_{1.92}Gd_{0.08}O_4$ at 300 K, can be related to superparamagnetic behavior of some particles of sizes below the critical size. The small value of squareness ratio, $SQR = 0.072$ for $x = 0.08$ demonstrates that the nanoparticles are relaxing so fast and act as superparamagnet at room temperature even in the absence of an external magnetic field [102].

The law of approach to saturation (LAS) plays a vital role in studying the magnetization processes and their variation with the magnetic field in high-field regions. To describe the behavior near saturation of the prepared $Mg_{0.33}Ni_{0.33}Co_{0.33}Fe_{2-x}Gd_xO_4$, where $x = 0.00, 0.01, 0.02, 0.04, \text{ and } 0.08$, the LAS was applied. To determine the most reliable model for obtaining information about magnetic parameters such as M_s and K , a study was conducted on three different LAS models applicable to various structures of spinel ferrites. LAS models, displayed in Fig. 8, are described in the following equations [103]:

$$\text{Model 1 : } M = M_s \left(1 - \frac{c}{H} - \frac{b}{H^2} \right) + \chi H \quad (10)$$

$$\text{Model 2 : } M = M_s \left(1 - \frac{c}{H} - \frac{b}{H^2} \right) \quad (11)$$

$$\text{Model 3 : } M = M_s \left(1 - \frac{b}{H^2} \right) + \chi H \quad (12)$$

where χH demonstrates the forced magnetization that grows up in magnetization with the magnetic field. The fitting parameter b indicates the variation

of magnetocrystalline anisotropy during the increase of the magnetic field. The term c/H shows an indication of the deformation in the lattice structure and c indicates the magnetic hardness and is related to the sample microstructure. Although these models could be applied for spinel ferrites, the particular type of magnetic material, the applied magnetic field range, and experimental conditions could affect the extracted results of magnetic parameters [103]. At low regions of the applied magnetic field, the magnetization includes domain wall motion whereas in high-field regions the magnetization process consists of the rotation of domains [104]. To ensure that the magnetization process is dominated by domain rotations rather than other factors such as domain wall motion and to obtain accurate results, the fitting of LAS models is often performed in the high-field regions, typically specified as $2000 < H < 20000$ [105].

To choose the suitable model for describing the dependency of the magnetic field at appropriate high-level regions and extracting acceptable values of magnetic parameters, a Mathematica 13.3 Wolfram coding package has been created. The values measured from the three models are listed in Table 5. From the fitting parameters, the magnetocrystalline anisotropy K can be calculated from equation [106]:

$$K = \mu_0 M_s \sqrt{\frac{105 b}{8}} \quad (13)$$

From Table 5, the decrease in the M_s values, calculated using LAS models, is comparable to the data extracted from hysteresis loops. The increase in parameter c with increasing the concentration of Gd^{3+} ions, as observed in Table 6, could be attributed to the substitution of Fe^{3+} ions (with an ionic radius of 0.645 Å) by Gd^{3+} ions (with a larger ionic radius of 0.938 Å). This substitution introduces structural defects within the material, leading to the observed increase in the c parameter. Moreover, the introduction of Gd^{3+} dopant in the crystal lattice can cause dislocations, which disrupt the alignment of magnetic domains and result in an increase in the magnetic hardness [107]. All the fitted LAS models exhibited high coefficient of determination (R^2) values. However, the LAS models, mainly $M = M_s \left(1 - \frac{c}{H} - \frac{b}{H^2} \right) + \chi H$ and $M = M_s \left(1 - \frac{c}{H} - \frac{b}{H^2} \right)$, reveal negative values of b in all the prepared samples. Thus, these models are not valid for calculating the

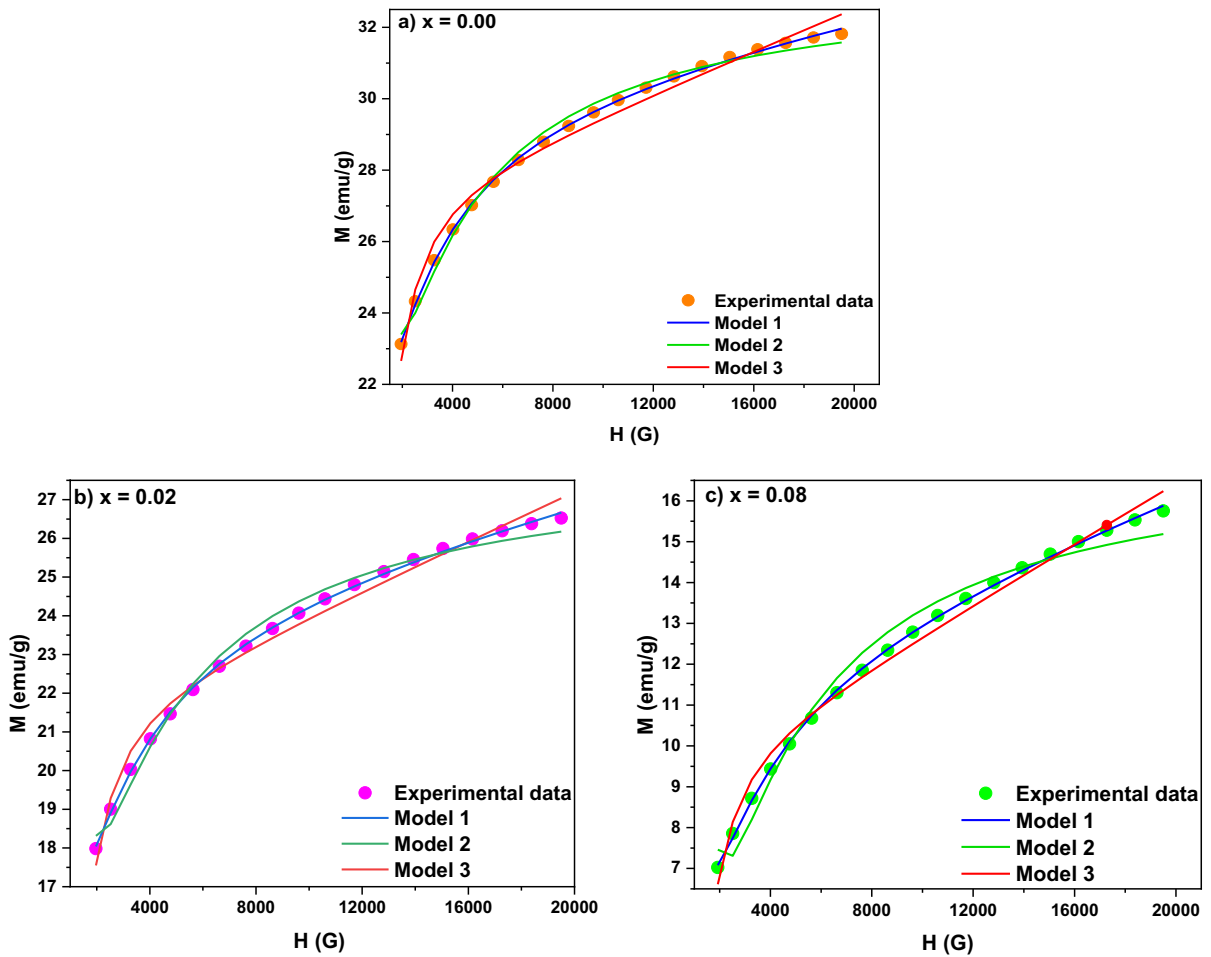


Fig. 8 Fitting plots of LAS models for $Mg_{0.33}Ni_{0.33}Co_{0.33}Fe_{2-x}Gd_xO_4$ where **a** $x = 0.00$, **b** $x = 0.02$, and **c** $x = 0.08$

Table 6 Parameters obtained from the fitting of LAS models in the field region $2000\text{ G} < H < 20000\text{ G}$ for $Mg_{0.33}Ni_{0.33}Co_{0.33}Fe_{2-x}Gd_xO_4$ where $x = 0.00, 0.02$, and 0.08

Model	Equation	Parameter	x		
			0.00	0.02	0.08
Model 1	$M = M_s \left(1 - \frac{c}{H} - \frac{b}{H^2} \right) + \chi H$	M_s (emu/g)	30.747	24.74	12.678
		c (G)	776.772	911.486	1651.096
		$b \times 10^6$ (G ²)	-0.548	-0.696	-1.41
		χ	0.00012	0.00015	0.00021
Model 2	$M = M_s \left(1 - \frac{c}{H} - \frac{b}{H^2} \right)$	M_s (emu/g)	33.347	28.153	17.397
		c (G)	1140.77	1446.88	2628.86
		$b \times 10^6$ (G ²)	-1.08	-1.49	-2.94
Model 3	$M = M_s \left(1 - \frac{b}{H^2} \right) + \chi H$	M_s (emu/g)	26.662	20.899	9.0724
		$b \times 10^6$ (G ²)	0.655	0.736	1.297
		χ	0.00029	0.00031	0.00036
		K	0.099	0.082	0.047

magnetocrystalline anisotropy K . By excluding the term c/H , the model $M = M_s \left(1 - \frac{b}{H^2}\right) + \chi H$ reveals reliable values of M_s , b , and χ that describe the decrease of M_s and K upon increasing the Gd^{3+} concentration which in turn matches the obtained experimental results.

Conclusion

In this study, the influence of Gd^{3+} doping on the structural, optical, and magnetic properties of $\text{Mg}_{0.33}\text{Ni}_{0.33}\text{Co}_{0.33}\text{Fe}_{2-x}\text{Gd}_x\text{O}_4$ was examined. The structural properties of the samples were examined by XRD, TEM, and HRTEM. As Gd^{3+} concentration increases from 0.00 to 0.08, the lattice parameter increases from 8.315 to 8.367 Å whereas the average particle size decreases from 27.5 to 14.2 nm, respectively. This was attributed to the difference in the ionic radii between the host Fe^{3+} (0.645 Å) and the dopant Gd^{3+} (0.938 Å) ions. Agglomeration among the prepared nanoparticles, revealed from TEM analysis, was owed to the magnetic interparticle interactions. Compared with previously published reports, smaller crystallite sizes are obtained upon doping nanoferrites with Gd^{3+} . Smaller nanoparticles have a higher surface area-to-volume ratio, which makes them good candidates for catalysis, adsorption, and surface modification applications. The optical properties studied by PL showed evidence of the existence of structural defects. The slowest recombination rate of electron-hole pair was revealed by $\text{Mg}_{0.33}\text{Ni}_{0.33}\text{Co}_{0.33}\text{Fe}_{2-x}\text{Gd}_x\text{O}_4$ nanoparticles with $x=0.08$. Thus, these nanoparticles can be used as photocatalysts for the degradation of pollutants and wastewater treatment. A shift in the peak position in the Raman modes revealed upon increasing Gd^{3+} concentrations was due to the large difference in reduced mass between the Fe^{3+} (55.85 g) and the Gd^{3+} (157.25 g) ions. The settling of Gd^{3+} dopant ions at the B site caused the migration of Fe^{3+} ions from the octahedral site to the tetrahedral site as revealed by Mössbauer spectra recorded at 77 K. In addition, the M_s values were reduced from 31.870 to 15.760 emu/g with the increase of Gd^{3+} concentration from 0.00 to 0.08, respectively. The small value of the squareness ratio, $\text{SQR} = 0.072$ for $x = 0.08$, demonstrates that the nanoparticles act as superparamagnets at room temperature. The relationship between

magnetization and the applied field was investigated by fitting the experimental data into different forms of the law of approach to saturation. The prepared $\text{Mg}_{0.33}\text{Ni}_{0.33}\text{Co}_{0.33}\text{Fe}_{2-x}\text{Gd}_x\text{O}_4$ nanoparticles exhibited unique structural, optical, and magnetic properties which could have a futuristic significance in industrial applications such as sensors, light-emitting diodes (LEDs), photocatalysts, and electric generators.

Acknowledgements This research was carried out in the Specialized Materials Science Lab and Advanced Nanomaterials Research Lab at Beirut Arab University in Lebanon in collaboration with Alexandria University in Egypt. Furthermore, the Mössbauer analysis was performed at the Université du Mans in France.

Author contribution Conceptualization: Ramadan Awad; data curation: Amani Aridi, Maraim Rabaa, and Ramy Moussa; formal analysis: Amani Aridi, Mariam Rabaa, Ramy Moussa, and Ramadan Awad; writing—original draft preparation: Amani Aridi, Maraim Rabaa, and Ramy Moussa; writing—review and editing: Amani Aridi, Mariam Rabaa, Ramy Moussa, Roudaina Sayed Hassan, Nader Yaacoub, and Ramadan Awad; resources: Roudaina Sayed Hassan, Nader Yaacoub, and Ramadan Awad; supervision: Ramadan Awad. All authors read and approved the final manuscript.

Data availability The data supporting the reported results are available upon request.

Compliance with ethical standard

Competing interests The authors declare no competing interests.

Ethics approval and consent to participate Not applicable.

References

- Gonçalves JM, de Faria LV, Nascimento AB, Germesheid RL, Patra S, Hernández-Saravia LP, Bonacin JA, Munoz RA, Angnes L (2022) Sensing performances of spinel ferrites MFe_2O_4 (M= Mg, Ni, Co, Mn, Cu and Zn) based electrochemical sensors: a review. *Anal Chim Acta* 1233:340362. <https://doi.org/10.1016/j.aca.2022.340362>
- Qin H, He Y, Xu P, Huang D, Wang Z, Wang H, Wang Z, Zhao Y, Tian Q, Wang C (2021) Spinel ferrites (MFe_2O_4): synthesis, improvement and catalytic application in environment and energy field. *Adv Colloid Interface Sci* 294:102486. <https://doi.org/10.1016/j.cis.2021.102486>
- Maensiri S, Sangmanee M, Wiengmoon A (2009) Magnetite ferrite (MgFe_2O_4) nanostructures fabricated by electrospinning. *Nanoscale Res Lett* 4:221–228. <https://doi.org/10.1007/s11671-008-9229-y>

4. Gunjekar JL, More AM, Gurav KV, Lokhande CD (2008) Chemical synthesis of spinel nickel ferrite (NiFe_2O_4) nano-sheets. *Appl Surf Sci* 254(18):5844–5848. <https://doi.org/10.1016/j.apsusc.2008.03.065>
5. Barvinschi P, Stefanescu O, Dippong T, Sorescu S, Stefanescu M (2013) $\text{CoFe}_2\text{O}_4/\text{SiO}_2$ nanocomposites by thermal decomposition of some complex combinations embedded in hybrid silica gels. *J Therm Anal Calorim* 112:447–453. <https://doi.org/10.1007/s10973-012-2704-9>
6. Dippong T, Levei EA, Borodi G, Goga F, Barbu Tudoran L (2015) Influence of Co/Fe ratio on the oxide phases in nanoparticles of $\text{Co}_x\text{Fe}_{3-x}\text{O}_4$. *J Therm Anal Calorim* 119:1001–1009. <https://doi.org/10.1007/s10973-014-4280-7>
7. Dippong T, Levei EA, Tanaselia C, Gabor M, Nasui M, Tudoran LB, Borodi G (2016) Magnetic properties evolution of the $\text{Co}_x\text{Fe}_{3-x}\text{O}_4/\text{SiO}_2$ system due to advanced thermal treatment at 700° C and 1000° C. *J Magn Magn Mater* 410:47–54. <https://doi.org/10.1016/j.jmmm.2016.03.020>
8. Mohamed R, Rashad MM, Haraz FA, Sigmund W (2010) Structure and magnetic properties of nanocrystalline cobalt ferrite powders synthesized using organic acid precursor method. *J Magn Magn Mater* 322(14):2058–2064. <https://doi.org/10.1016/j.jmmm.2010.01.034>
9. Velhal NB, Patil ND, Shelke AR, Deshpande NG, Puri VR (2015) Structural, dielectric and magnetic properties of nickel substituted cobalt ferrite nanoparticles: effect of nickel concentration. *AIP Adv* 5(9):097166. <https://doi.org/10.1063/1.4931908>
10. Shobana MK, Rajendran V, Jeyasubramanian K, Kumar NS (2007) Preparation and characterisation of NiCo ferrite nanoparticles. *Mater Lett* 61(13):2616–2619. <https://doi.org/10.1016/j.matlet.2006.10.008>
11. Vinayak V, Khirade PP, Birajdar SD, Sable DB, Jadhav KM (2016) Structural, microstructural, and magnetic studies on magnesium (Mg^{2+})-substituted CoFe_2O_4 nanoparticles. *J Supercond Nov Magn* 29:1025–1032. <https://doi.org/10.1007/s10948-015-3348-3>
12. Mohammad AM, Aliridha SM, Mubarak TH (2018) Structural and magnetic properties of mg-co ferrite nanoparticles. *Dig. J. Nanomater. Biostructures* 13(3):615–623
13. Anumol CN, Chithra M, Rout S, Sahoo SC (2020) Effect of Magnesium substitution on structural and magnetic properties of Nickel ferrite nanoparticles. *J Supercond Nov Magn* 33:1611–1617. <https://doi.org/10.1007/s10948-019-05192-8>
14. Ashrafzadeh A, Ghasemi A, Paesano A Jr, Machado CF, Liu X, Morisako A (2010) Structural and magnetic properties of $\text{Cu}_x\text{Mg}_{0.5-x}\text{Zn}_{0.5}\text{Fe}_2\text{O}_4$ ($x = 0-0.5$) particles. *J Alloys Compd* 506(1):279–284. <https://doi.org/10.1016/j.jallcom.2010.06.191>
15. Suo N, Sun A, Zhang Y, Yu L, Shao L, Zuo Z (2021) Magnetic transformation of Ni–Mg–Zn ferrite substituted by the Co^{2+} ions from soft magnetic to hard magnetic. *J Mater Sci: Mater Electron* 32:3286–3302. <https://doi.org/10.1007/s10854-020-05077-w>
16. Suo N, Sun A, Yu L, Zuo Z, Zhao X, Zhang W, Zhang Y, Shao L, Yu T (2020) Preparation and study of lattice structure and magnetic properties of Bi^{3+} ion-doped Ni–Mg–Co ferrites by sol–gel auto-combustion method. *J Sol-Gel Sci Technol* 95:360–374. <https://doi.org/10.1007/s10971-020-05302-2>
17. Tanbir K, Ghosh MP, Singh RK, Kar M, Mukherjee S (2020) Effect of doping different rare earth ions on microstructural, optical, and magnetic properties of nickel–cobalt ferrite nanoparticles. *J Mater Sci: Mater Electron* 31:435–343. <https://doi.org/10.1007/s10854-019-02546-9>
18. Ansari MM, Khan S, Ahmad N (2018) Effect of R^{3+} ($\text{R} = \text{Pr, Nd, Eu and Gd}$) substitution on the structural, electrical, magnetic and optical properties of Mn-ferrite nanoparticles. *J Magn Magn Mater* 465:81–87. <https://doi.org/10.1016/j.jmmm.2018.05.071>
19. Sinha A, Dutta A (2020) Structural, optical, and electrical transport properties of some rare-earth-doped nickel ferrites: a study on effect of ionic radii of dopants. *J Phys Chem Solids* 145:109534. <https://doi.org/10.1016/j.jpcs.2020.109534>
20. Ikram S, Ashraf F, Alzaid M, Mahmood K, Amin N, Haider SA (2021) Role of nature of rare earth ion dopants on structural, spectral, and magnetic properties in spinel ferrites. *J Supercond Nov Magn* 34:1745–1751. <https://doi.org/10.1007/s10948-020-05723-8>
21. Li S, Pan J, Gao F, Zeng D, Qin F, He C, Dodbiba G, Wei Y, Fujita T (2021) Structure and magnetic properties of coprecipitated nickel-zinc ferrite-doped rare earth elements of Sc, Dy, and Gd. *J Mater Sci: Mater Electron* 32:13511–13526. <https://doi.org/10.1007/s10854-021-05928-0>
22. Shao L, Sun A, Zhang Y, Yu L, Suo N, Zuo Z (2021) Comparative study on the structure and magnetic properties of Ni–Mg–Co ferrite doped with Al and rare earth elements. *J Mater Sci: Mater Electron* 32:5339–5352. <https://doi.org/10.1007/s10854-020-05161-1>
23. Yu L, Sun A, Suo N, Zuo Z, Zhao X, Zhang W, Shao L, Zhang Y (2020) Enhancement of magnetic properties of Ni–Mg–Co ferrites by Y^{3+} ions doping. *J Mater Sci: Mater Electron* 31:14961–14976. <https://doi.org/10.1007/s10854-020-04059-2>
24. Arshad J, Alzahrani FM, Munir S, Younis U, Al-Buriah MS, Alrowaili ZA, Warsi MF (2023) Integration of 2D graphene oxide sheets with $\text{MgFe}_2\text{O}_4/\text{ZnO}$ heterojunction for improved photocatalytic degradation of organic dyes and benzoic acid. *Ceram Int* 49(11):18988–19002. <https://doi.org/10.1016/j.ceramint.2023.03.024>
25. Wangchhuk J, Meher SR (2022) Structural, electronic and magnetic properties of inverse spinel NiFe_2O_4 : DFT + U investigation. *Phys Lett A* 443:128202. <https://doi.org/10.1016/j.physleta.2022.128202>
26. Al Maashani MS, Khalaf KA, Gismelseed AM, Al-Omari IA (2020) The structural and magnetic properties of the nano- CoFe_2O_4 ferrite prepared by sol-gel auto-combustion technique. *J Alloys Compd* 817:152786. <https://doi.org/10.1016/j.jallcom.2019.152786>
27. Dippong T, Levei EA, Cadar O (2017) Preparation of $\text{CoFe}_2\text{O}_4/\text{SiO}_2$ nanocomposites at low temperatures using short chain diols. *J Chem* 2017:7943164. <https://doi.org/10.1155/2017/7943164>

28. Dippong T, Levei EA, Cadar O, Goga F, Borodi G, Barbu-Tudoran L (2017) Thermal behavior of $\text{Co}_x\text{Fe}_{3-x}\text{O}_4/\text{SiO}_2$ nanocomposites obtained by a modified sol-gel method. *J Therm Anal Calorim* 128:39–52. <https://doi.org/10.1007/s10973-016-5930-8>
29. Jiang J, Li L, Xu F, Xie Y (2007) Preparation and magnetic properties of Zn-Cu-Cr-Sm ferrite via a rheological phase reaction method. *Mater Sci Eng B* 137(1-3):166–169. <https://doi.org/10.1016/j.mseb.2006.11.014>
30. Hashim M, Shirsath SE, Kumar S, Kumar R, Roy AS, Shah J, Kotnala RK (2013) Preparation and characterization chemistry of nano-crystalline Ni-Cu-Zn ferrite. *J Alloys Compd* 549:348–357. <https://doi.org/10.1016/j.jallcom.2012.08.039>
31. Poudel TP, Rai BK, Yoon S, Guragain D, Neupane D, Mishra SR (2019) The effect of gadolinium substitution in inverse spinel nickel ferrite: structural, magnetic, and Mössbauer study. *J Alloys Compd* 802:609–619. <https://doi.org/10.1016/j.jallcom.2019.06.201>
32. Kadam A, Mande VK, Kadam S, Kadam R, Shirsath SE, Borade RB (2020) Influence of gadolinium (Gd^{3+}) ion substitution on structural, magnetic and electrical properties of cobalt ferrites. *J Alloys Compd* 840:155669. <https://doi.org/10.1016/j.jallcom.2020.155666>
33. Yadav RS, Kuřitka I, Vilcakova J, Havlica J, Kalina L, Urbánek P, Machovsky M, Skoda D, Masař M (2018) Influence of Gd^{3+} -substitution on structural, magnetic, dielectric and modulus spectroscopic characteristics of ZnFe_2O_4 spinel ferrite nanoparticles. *J Mat Sci: Mater Electron* 29:15878–15893. <https://doi.org/10.1007/s10854-018-9674-z>
34. Kanna RR, Sakthipandi K, Maraikkayar SS, Lenin N, Sivabharathy M (2018) Doping effect of rare-earth (lanthanum, neodymium and gadolinium) ions on structural, optical, dielectric and magnetic properties of copper nanoferrites. *J Rare Earths*. 36(12):1299–1309. <https://doi.org/10.1016/j.jre.2018.03.033>
35. Hussain K, Bibi A, Jabeen F, Amin N, Mahmood K, Ali A, Iqbal MZ, Arshad MI (2020) Study of structural, optical, electrical and magnetic properties of Cu^{2+} doped $\text{Zn}_{0.4}\text{Co}_{0.6-x}\text{Ce}_{0.1}\text{Fe}_{1.9}\text{O}_4$ spinel ferrites. *Phys B: Condens Matter* 584:412078. <https://doi.org/10.1016/j.physb.2020.412078>
36. Kumar P, Pathak S, Singh A, Jain K, Khanduri H, Wang L, Kim SK, Pant RP (2022) Observation of intrinsic fluorescence in cobalt ferrite magnetic nanoparticles by Mn^{2+} substitution and tuning the spin dynamics by cation distribution. *J Mater Chem C* 10(35):12652–12679. <https://doi.org/10.1039/D2TC02605H>
37. Basma H, Al Boukhari J, Abd Al Nabi M, Aridi A, Sayed Hassan R, Naoufal D, Roumie M, Awad R (2022) Enhancement of the magnetic and optical properties of $\text{Ni}_{0.5}\text{Zn}_{0.5}\text{Fe}_2\text{O}_4$ nanoparticles by ruthenium doping. *Appl Phys A* 128(5):409. <https://doi.org/10.1007/s00339-022-05552-7>
38. Fontaine F, Christidis GE, Yans J, Hollanders S, Hoffman A, Fagel N (2020) Characterization and origin of two Fe-rich bentonites from Westerwald (Germany). *Appl Clay Sci* 187:105444. <https://doi.org/10.1016/j.clay.2020.105444>
39. Owolabi TO, Saleh TA, Olusayo O, Souiyah M, Oyeneyin OE (2021) Modeling the specific surface area of doped spinel ferrite nanomaterials using hybrid intelligent computational method. *J Nanomater* 2021:1–13. <https://doi.org/10.1155/2021/9677423>
40. Kumar D, Kumar A, Prakash R, Singh AK (2019) X-ray diffraction analysis of Cu^{2+} doped $\text{Zn}_{1-x}\text{Cu}_x\text{Fe}_2\text{O}_4$ spinel nanoparticles using Williamson-Hall plot method. *AIP Conf Proc* 2142:070018. <https://doi.org/10.1063/1.5122410>
41. Ghosh MP, Mandal S, Mukherjee S (2020) Correlations between microstructural and magnetic properties of Gd^{3+} -doped spinel ferrite nanoparticles. *Eur Phys J Plus* 135(1):41. <https://doi.org/10.1140/epjp/s13360-020-00112-5>
42. Liu R, Sun H, Liu X, Yan W, Jiang X (2022) Effect of Gd on microstructure, mechanical properties and damping properties of Fe-Cr-Al alloys. *Mater Charact* 187:111841. <https://doi.org/10.1016/j.matchar.2022.111841>
43. Anwar H, Maqsood A (2013) Enhancement of electrical and magnetic properties of Cd^{2+} doped Mn-Zn soft nanoferrites prepared by the sol-gel autocombustion method. *J Magn Magn Mater* 333:46–52. <https://doi.org/10.1016/j.jmmm.2012.12.027>
44. Bharati VA, Somvanshi SB, Humbe AV, Murumkar VD, Sondur VV, Jadhav KM (2020) Influence of trivalent Al-Cr co-substitution on the structural, morphological and Mössbauer properties of nickel ferrite nanoparticles. *J Alloys Compd* 821:153501. <https://doi.org/10.1016/j.jallcom.2019.153501>
45. Somvanshi SB, Khedkar MV, Kharat PB, Jadhav K (2020) Influential diamagnetic magnesium (Mg^{2+}) ion substitution in nano-spinel zinc ferrite (ZnFe_2O_4): thermal, structural, spectral, optical and physisorption analysis. *Ceram Int* 46(7):8640–8650. <https://doi.org/10.1016/j.ceramint.2019.12.097>
46. Islam M, Khan MKR, Kumar A, Rahman MM, Abdullah-Al-Mamun M, Rashid R, Haque MM, Sarker MSI (2022) Sol-gel route for the synthesis of $\text{CoFe}_{2-x}\text{Er}_x\text{O}_4$ nanocrystalline ferrites and the investigation of structural and magnetic properties for magnetic device applications. *ACS Omega* 7(24):20731–20740. <https://doi.org/10.1021/acsomega.2c00982>
47. Sarker M, Yeasmin M, Al-Mamun MA, Hoque SM, Khan MK (2022) Influence of Gd content on the structural, Raman spectroscopic and magnetic properties of CoFe_2O_4 nanoparticles synthesized by sol-gel route. *Ceram Int* 48(22):33323–33331. <https://doi.org/10.1016/j.ceramint.2022.07.27>
48. Yao H, Ning X, Zhao H, Hao A, Ismail M (2021) Effect of Gd-doping on structural, optical, and magnetic properties of NiFe_2O_4 as-prepared thin films via facile sol-gel approach. *ACS Omega* 6(9):6305–6311. <https://doi.org/10.1021/acsomega.0c06097>
49. Parray IA, Somvanshi A, Naseem S, Hashim M, Khan W, Ali SA (2020) Microstructural and dielectric relaxation study of Gd^{3+} ion substituted MgFe_2O_4 . *AIP Conf Proc* 2265:030114. <https://doi.org/10.1063/5.0018111>
50. de Medeiros F, Madigou V, Lopes-Moriyama AL, de Souza CP, Leroux C (2020) Synthesis of CoFe_2O_4

- nanocubes. *Nano-Struct Nano-Objects* 21:100422. <https://doi.org/10.1016/j.nanoso.2019.100422>
51. Geetha K, Udhayakumar R, Manikandan A (2021) Enhanced magnetic and photocatalytic characteristics of cerium substituted spinel MgFe_2O_4 ferrite nanoparticles. *Phys B: Condens Matter* 615:413083. <https://doi.org/10.1016/j.physb.2021.413083>
 52. Hariharasuthan R, Chitradevi S, Radha KS, Chithambaram V (2022) Characterization of NiFe_2O_4 (nickel ferrite) nanoparticles with very low magnetic saturation synthesized via co-precipitation method. *Appl Phys A* 128:1045. <https://doi.org/10.1007/s00339-022-06163-y>
 53. Yousaf M, Nazir S, Akbar M, Akhtar MN, Noor A, Hu E, Shah MY, Lu Y (2022) Structural, magnetic, and electrical evaluations of rare earth Gd^{3+} doped in mixed Co-Mn spinel ferrite nanoparticles. *Ceram Int* 48(1):578–586. <https://doi.org/10.1016/j.ceramint.2021.09.136>
 54. Al Bitar M, Khalil M, Awad R (2022) Effect of La^{3+} and Ce^{3+} dopant ions on structural, optical, magnetic, and antibacterial activity of ZnO nanoparticles. *Mater Today Commun* 33:104683. <https://doi.org/10.1016/j.mtcomm.2022.104683>
 55. Bitar Z, Isber S, Noureddine S, Bakeer DE, Awad R (2017) Synthesis, characterization, optical properties, and electron paramagnetic resonance for nano $\text{Zn}_{0.5}\text{Co}_{0.5}\text{Fe}_{2-x}\text{Pr}_x\text{O}_4$. *J Supercond Nov Magn* 30:3603–3609. <https://doi.org/10.1007/s10948-016-3873-8>
 56. Aridi A, Awad R, Khalaf A (2021) Synthesis and characterization of $\text{ZnFe}_2\text{O}_4/\text{Mn}_2\text{O}_3$ nanocomposites. *Appl Phys A* 127:206. <https://doi.org/10.1007/s00339-021-04362-7>
 57. Ghosh MP, Mukherjee S (2019) Microstructural, magnetic, and hyperfine characterizations of Cu-doped cobalt ferrite nanoparticles. *J Am Ceram Soc* 102(12):7509–7520. <https://doi.org/10.1111/jace.16687>
 58. Gupta R, Sood AK, Metcalf P, Honig JM (2002) Raman study of stoichiometric and Zn-doped Fe_3O_4 . *Phys Rev B* 65(10):104430. <https://doi.org/10.1103/PhysRevB.65.104430>
 59. Nekvapil F, Bunge A, Radu T, Cinta Pinzaru S, Turcu R (2020) Raman spectra tell us so much more: Raman features and saturation magnetization for efficient analysis of manganese zinc ferrite nanoparticles. *J Raman Spectrosc* 51(6):959–968. <https://doi.org/10.1002/jrs.5852>
 60. Aslam A, Morley NA, Amin N, Arshad MI, un Nabi MA, Ali A, Mahmood K, Bibi A, Iqbal F, Hussain S, Jamil Y (2021) Study of structural, optical and electrical properties of La^{3+} doped $\text{Mg}_{0.25}\text{Ni}_{0.15}\text{Cu}_{0.25}\text{Co}_{0.35}\text{Fe}_{2-x}\text{La}_x\text{O}_4$ spinel ferrites. *Phys B: Condens Matter* 602:412565. <https://doi.org/10.1016/j.physb.2020.412565>
 61. Ansari SM, Ghosh KC, Devan RS, Sen D, Sastry PU, Kolekar YD, Ramana CV (2020) Eco-friendly synthesis, crystal chemistry, and magnetic properties of manganese-substituted CoFe_2O_4 nanoparticles. *ACS Omega* 5(31):19315–19330. <https://doi.org/10.1021/acsomega.9b02492>
 62. Zhang S, Wu J, Li F, Li L (2022) Enhanced photocatalytic performance of spinel ferrite (MFe_2O_4 , M= Zn, Mn, Co, Fe, Ni) catalysts: the correlation between morphology–microstructure and photogenerated charge efficiency. *J Environ Chem Eng* 10(3):107702. <https://doi.org/10.1016/j.jece.2022.107702>
 63. Manohar A, Krishnamoorthi C, Naidu KCB, Pavithra C (2019) Dielectric, magnetic hyperthermia, and photocatalytic properties of ZnFe_2O_4 nanoparticles synthesized by solvothermal reflux method. *Appl Phys A* 125:1–10. <https://doi.org/10.1007/s00339-019-2760-0>
 64. Kefeni KK, Msagati TA, Mamba BB (2017) Ferrite nanoparticles: synthesis, characterisation and applications in electronic device. *Mater Sci Eng B* 215:37–55. <https://doi.org/10.1016/j.mseb.2016.11.002>
 65. Puli VS, Adireddy S, Ramana CV (2015) Chemical bonding and magnetic properties of gadolinium (Gd) substituted cobalt ferrite. *J Alloys Compd* 644:470–475. <https://doi.org/10.1016/j.jallcom.2015.05.031>
 66. Nandan B, Bhatnagar MC, Kashyap SC (2019) Cation distribution in nanocrystalline cobalt substituted nickel ferrites: X-ray diffraction and Raman spectroscopic investigations. *J Phys Chem Solids* 129:298–306. <https://doi.org/10.1016/j.jpcs.2019.01.017>
 67. Granone LI, Ulpe AC, Robben L, Klimke S, Jahns M, Renz F, Gesing TM, Bredow T, Dillert R, Bahnemann DW (2018) Effect of the degree of inversion on optical properties of spinel ZnFe_2O_4 . *Phys Chem Chem Phys* 20(44):28267–28278. <https://doi.org/10.1039/C8CP05061A>
 68. Yan Z, Gao J, Li Y, Zhang M, Guo M (2015) Hydrothermal synthesis and structure evolution of metal-doped magnesium ferrite from saprolite laterite. *RCS Adv* 5(112):92778–92787. <https://doi.org/10.1039/C5RA17145H>
 69. Massoudi J, Smari M, Nouri K, Dhahri E, Khirouni K, Bertaina S, Bessais L (2020) Magnetic and spectroscopic properties of Ni–Zn–Al ferrite spinel: from the nanoscale to microscale. *RSC Adv* 10(57):34556–34580. <https://doi.org/10.1039/D0RA05522K>
 70. Ghorbani H, Eshraghi M, Dodaran AS, Kameli P, Protasowicki S, Vashae D (2022) Effect of Yb doping on the structural and magnetic properties of cobalt ferrite nanoparticles. *Mat Res Bull* 147:111642. <https://doi.org/10.1016/j.materresbull.2021.111642>
 71. Dar MI, Shivashankar SA (2014) Single crystalline magnetite, maghemite, and hematite nanoparticles with rich coercivity. *RSC Adv* 4(8):4105–4113. <https://doi.org/10.1039/C3RA45457F>
 72. Chamritski I, Burns G (2005) Infrared-and Raman-active phonons of magnetite, maghemite, and hematite: a computer simulation and spectroscopic study. *J Phys Chem B* 109(11):4965–4968. <https://doi.org/10.1021/jp048748h>
 73. Qureshi AA, Javed S, Javed HMA, Jamshaid M, Ali U, Akram MA (2022) Systematic investigation of structural, morphological, thermal, optoelectronic, and magnetic properties of high-purity hematite/magnetite nanoparticles for optoelectronics. *Nanomaterials* 12(10):1635. <https://doi.org/10.3390/nano12101635>
 74. Raj AM, Chirayil GT (2017) Tunable direct band gap photoluminescent organic semiconducting nanoparticles from lignite. *Sci Rep* 7(1):18012. <https://doi.org/10.1038/s41598-017-18338-2>
 75. Arif M, Sanger A, Shkir M, Singh A, Katiyar RS (2019) Influence of interparticle interaction on the structural, optical and magnetic properties of NiO nanoparticles. *Phys B: Condens Matter* 552:88–95. <https://doi.org/10.1016/j.physb.2018.09.023>

76. Harzali H, Marzouki A, Saida F, Megriche A, Mgaidi A (2018) Structural, magnetic and optical properties of nanosized $\text{Ni}_{0.4}\text{Cu}_{0.2}\text{Zn}_{0.4}\text{R}_{0.05}\text{Fe}_{1.95}\text{O}_4$ (R = Eu^{3+} , Sm^{3+} , Gd^{3+} and Pr^{3+}) ferrites synthesized by co-precipitation method with ultrasound irradiation. *J Magn Magn Mater* 460:89–94. <https://doi.org/10.1016/j.jmmm.2018.03.062>
77. Devi EC, Singh SD (2023) Magnetic and photoluminescence properties of rare-earth substituted quaternary spinel ferrite nanoparticles. *Ceram Int* 49(5):8409–8416. <https://doi.org/10.1016/j.ceramint.2022.11.003>
78. Lin Q, Yang F, Zhang Q, Su K, Xu H, He Y, Lin J (2023) Mössbauer and structure-magnetic properties analysis of $\text{A}_y\text{B}_{1-y}\text{C}_x\text{Fe}_{2-x}\text{O}_4$ (C = Ho, Gd, Al) ferrite nanoparticles optimized by doping. *Molecules* 28(10):4226. <https://doi.org/10.3390/molecules28104226>
79. Yassine R, Abdallah A, Hassan RS, Yaacoub N, Awad R, Bitar Z (2022) Physical properties of nanosized (x) NiO/(1-x)CdFe₂O₄ composites. *Ceram Int* 48(10):14825–14838. <https://doi.org/10.1016/j.ceramint.2022.02.019>
80. Yehia M, Hashhash A (2019) Structural and magnetic study of Sm doped NiFe₂O₄ nanoparticles. *J Mater Sci: Mater Electron* 30:6768–6775. <https://doi.org/10.1007/s10854-019-00988-9>
81. Al-Mokdad F, Bitar Z, Hassan RS, Yaacoub N, Awad R (2020) Effect of molybdenum doping on the structural and magnetic properties of MnFe₂O₄ magnetic nanoparticles. *Appl Phys A* 126:495. <https://doi.org/10.1007/s00339-020-03687-z>
82. Lakshman A, Rao PS, Rao KH (2006) Mössbauer spectroscopic analyses of $\text{Mg}_{0.9}\text{Cu}_{0.1}\text{Mn}_{0.05}\text{Cr}_x\text{Fe}_{1.95-x}\text{O}_4$ spinel ferrites. *Mater Lett* 60(1):7–10. <https://doi.org/10.1016/j.matlet.2005.07.043>
83. Patange S, Desai S, Meena S, Yusuf S, Shirsath SE (2015) Random site occupancy induced disordered Néel-type collinear spin alignment in heterovalent Zn^{2+} - Ti^{4+} ion substituted CoFe₂O₄. *RSC Adv* 5:91482–91492. <https://doi.org/10.1039/C5RA21522F>
84. Ata-Allah SS, Fayek MK, Yehia M (2004) Mössbauer and DC electrical resistivity study of Zn substituted tetragonal $\text{CuFe}_{2-y}\text{Ga}_y\text{O}_4$ compound. *J Mag Magn Mater* 279:411–420. <https://doi.org/10.1016/j.jmmm.2004.02.011>
85. He Y, Yang X, Lin J, Lin Q, Dong J (2015) Mössbauer spectroscopy, structural and magnetic studies of Zn^{2+} substituted magnesium ferrite nanomaterials prepared by Sol-Gel method. *J Nanomater* 2015:854840. <https://doi.org/10.1155/2015/854840>
86. Naaz F, Dubey HK, Kumari C, Lahiri P (2020) Structural and magnetic properties of MgFe₂O₄ nanopowder synthesized via co-precipitation route. *SN Appl Sci* 2(5):808. <https://doi.org/10.1007/s42452-020-2611-9>
87. Chandekar KV, Yadav SP, Chinke S, Shkir M (2023) Impact of Co-doped NiFe₂O₄ ($\text{Co}_x\text{Ni}_{1-x}\text{Fe}_2\text{O}_4$) nanostructures prepared by co-precipitation route on the structural, morphological, surface, and magnetic properties. *J Alloys Compd* 966:171556. <https://doi.org/10.1016/j.jallcom.2023.171556>
88. Agboola PO, Haider S, Shakir I (2022) The impact of rare earth Nd^{3+} cations on structural, spectral, magnetic and dielectric parameters of NiFe₂O₄ nanoparticles. *J Taibah Univ Sci* 16(1):392–400. <https://doi.org/10.1080/16583655.2022.2059953>
89. Ahmad SI, Ansari SA, Kumar DR (2018) Structural, morphological, magnetic properties and cation distribution of Ce and Sm co-substituted nano crystalline cobalt ferrite. *Mater Chem Phys* 208:248–257. <https://doi.org/10.1016/j.matchemphys.2018.01.050>
90. Hossain MD, Jamil AT, Hossain MS, Ahmed SJ, Das HN, Rashid R, Hakim MA, Khan MN (2022) Investigation on structure, thermodynamic and multifunctional properties of Ni–Zn–Co ferrite for Gd³⁺ substitution. *RSC Adv* 12(8):4656–4671. <https://doi.org/10.1039/D1RA04762K>
91. Belaiche Y, Minaoui K, Ouadou M, Elansary M, Ferdi CA (2021) New nanosized (Gd³⁺, Sm³⁺) co-doped zinc ferrite: structural, magnetic and first-principles study. *Phys B: Condens Matter* 619:413262. <https://doi.org/10.1016/j.physb.2021.413262>
92. Jacob BP, Thankachan S, Xavier S, Mohammed E (2011) Effect of Gd³⁺ doping on the structural and magnetic properties of nanocrystalline Ni–Cd mixed ferrite. *Phys Scr* 84(4):045702. <https://doi.org/10.1088/0031-8949/84/04/045702>
93. Peng J, Hojamberdiev M, Xu Y, Cao B, Wang J, Wu H (2011) Hydrothermal synthesis and magnetic properties of gadolinium-doped CoFe₂O₄ nanoparticles. *J Magn Magn Mater* 323(1):133–137. <https://doi.org/10.1016/j.jmmm.2010.08.048>
94. Narang SB, Pubby K (2021) Nickel spinel ferrites: a review. *J Magn Magn Mater* 519:167163. <https://doi.org/10.1016/j.jmmm.2020.167163>
95. Dippong T, Deac IG, Cadar O, Levei EA (2021) Effect of silica embedding on the structure, morphology and magnetic behavior of $(\text{Zn}_{0.6}\text{Mn}_{0.4}\text{Fe}_2\text{O}_4)_x(\text{SiO}_2)_{(100-x)}$ nanoparticles. *Nanomaterials* 11(9):2232. <https://doi.org/10.3390/nano11092232>
96. Murugesan C, Sathyamoorthy B, Chandrasekaran G (2015) Structural, dielectric and magnetic properties of Gd substituted manganese ferrite nanoparticles. *Phys Scr* 90(8):085809. <https://doi.org/10.1088/0031-8949/90/8/085809>
97. Stoner EC, Wohlfarth E (1948) A mechanism of magnetic hysteresis in heterogeneous alloys. *Philos Trans Royal Soc London Ser A Math Phys Eng Sci* 240(826):599–642. <https://doi.org/10.1098/rsta.1948.0007>
98. Mugutkar AB, Gore SK, Mane RS, Batoo KM, Adil SF, Jadhav SS (2018) Magneto-structural behaviour of Gd doped nanocrystalline Co-Zn ferrites governed by domain wall movement and spin rotations. *Ceram Int* 44(17):21675–21683. <https://doi.org/10.1016/j.ceramint.2018.08.255>
99. Tholkappian R, Vishista K (2015) Combustion synthesis of Mg–Er ferrite nanoparticles: cation distribution and structural, optical, and magnetic properties. *Mater Sci Semicond Process* 40:631–642. <https://doi.org/10.1016/j.mssp.2015.06.076>
100. Kadam R, Desai K, Shinde VS, Hashim M, Shirsath SE (2016) Influence of Gd³⁺ ion substitution on the MnCrFeO₄ for their nanoparticle shape formation and magnetic properties. *J Alloys Compd* 657:487–494. <https://doi.org/10.1016/j.jallcom.2015.10.164>
101. Dippong T, Levei EA, Cadar O, Deac IG, Lazar M, Borodi G et al (2020) Effect of amorphous SiO₂ matrix on structural and magnetic properties of $\text{Cu}_{0.6}\text{Co}_{0.4}\text{Fe}_2\text{O}_4$

- SiO₂ nanocomposites. *J Alloys Compd* 849:156695. <https://doi.org/10.1016/j.jallcom.2020.156695>
102. Jahan N, Uddin M, Khan M, Chowdhury F-U-Z, Hasan M, Das H et al (2021) Impact of particle size on the magnetic properties of highly crystalline Yb³⁺ substituted Ni–Zn nanoferrites. *J Mater Sci: Mater Electron* 32(12):16528–16543. <https://doi.org/10.1007/s10854-021-06209-6>
 103. Devi EC, Singh SD (2021) Tracing the magnetization curves: a review on their importance, strategy, and outcomes. *J Supercond Nov Magn* 34:15–25. <https://doi.org/10.1007/s10948-020-05733-6>
 104. Devi EC, Soibam I (2019) Law of approach to saturation in Mn–Zn ferrite nanoparticles. *J Supercond Nov Magn* 32:1293–1298. <https://doi.org/10.1007/s10948-018-4823-4>
 105. Frajer G, Isnard O, Chazal H, Delette G (2019) Effect of cobalt addition on the magneto-crystalline anisotropy parameter of sintered NiZn ferrites evaluated from magnetization curves. *J Magn Magn Mater* 473:92–98. <https://doi.org/10.1016/j.jmmm.2018.10.030>
 106. Chanu LP, Phanjoubam S (2023) On the structural and magnetic properties of Sr-substituted LaMnO₃ nanoparticles (La_{1-x}Sr_xMnO₃). *Mater Today: Proc.* <https://doi.org/10.1016/j.matpr.2023.04.621>
 107. Devi EC, Soibam I (2019) Magnetic properties and law of approach to saturation in Mn–Ni mixed nanoferrites. *J Alloys and Compd* 772:920–924. <https://doi.org/10.1016/j.jallcom.2018.09.160>

Publisher's Note Springer Nature remains neutral with regard to jurisdictional claims in published maps and institutional affiliations.

Springer Nature or its licensor (e.g. a society or other partner) holds exclusive rights to this article under a publishing agreement with the author(s) or other rightsholder(s); author self-archiving of the accepted manuscript version of this article is solely governed by the terms of such publishing agreement and applicable law.